J. Fluid Mech. (1991), *vol.* 233, *pp.* 299–328
Printed in Great Britain

Numerical simulations of three-dimensional thermal convection in a fluid with strongly temperature-dependent viscosity

By MASAKI OGAWA[1], GERALD SCHUBERT[2] AND ABDELFATTAH ZEBIB[3]

[1] Department of Earth Sciences, Ehime University, Ehime, 790, Japan

[2] Department of Earth and Space Sciences and Institute of Geophysics and Planetary Physics, University of California, Los Angeles, CA 90024, USA

[3] Department of Mechanical and Aerospace Engineering, Rutgers University, New Brunswick, NJ 08903, USA

(Received 20 August 1990 and in revised form 22 May 1991)

Numerical calculations are presented for the steady three-dimensional structure of thermal convection of a fluid with strongly temperature-dependent viscosity in a bottom-heated rectangular box. Viscosity is assumed to depend on temperature T as $\exp(-ET)$, where E is a constant; viscosity variations across the box $r(=\exp(E))$ as large as 10^5 are considered. A stagnant layer or lid of highly viscous fluid develops in the uppermost coldest part of the top cold thermal boundary layer when $r > r_{c1}$, where $r = r_{c1} \equiv 1.18 \times 10^3 R_t^{0.309}$ and R_t is the Rayleigh number based on the viscosity at the top boundary. Three-dimensional convection occurs in a rectangular pattern beneath this stagnant lid. The planform consists of hot upwelling plumes at or near the centre of a rectangle, sheets of cold sinking fluid on the four sides, and cold sinking plume concentrations immersed in the sheets. A stagnant lid does not develop, i.e. convection involves all of the fluid in the box when $r < r_{c1}$. The whole-layer mode of convection occurs in a three-dimensional bimodal pattern when $r > r_{c2} \equiv 3.84 \times 10^6 R_t^{-1.35}$. The planform of the convection is rectangular with the coldest parts of the sinking fluid and the hottest part of the upwelling fluid occurring as plumes at the four corners and at the centre of the rectangle, respectively. Both hot uprising plumes and cold sinking plumes have sheet-like extensions, which become more well-developed as r increases. The whole-layer mode of convection occurs as two-dimensional rolls when $r < \min(r_{c1}, r_{c2})$. The Nusselt number Nu depends on the viscosity at the top surface more strongly in the regime of whole-layer convection than in the regime of stagnant-lid convection. In the whole-layer convective regime, Nu depends more strongly on the viscosity at the top surface than on the viscosity at the bottom boundary.

1. Introduction

One of the most important characteristics of subsolidus convection in the mantles of terrestrial planets is the strong temperature-dependence of the rheology (Weertman 1970). Here, we study how this strong rheological temperature-dependence could affect the nature of mantle convection by numerically modelling the three-dimensional thermal convection of an infinite Prandtl number Boussinesq fluid with exponentially temperature-dependent viscosity in a rectangular box.

Several workers have carried out two-dimensional numerical simulations of thermal convection of infinite Prandtl number, strongly temperature-dependent viscosity fluids (for a review and literature summary, see Hager & Gurnis 1987). These studies have clarified how the strong temperature-dependence of viscosity affects the efficiency of convective heat transport (e.g. Christensen 1984*a*). An important feature of two-dimensional convection with strongly temperature-dependent viscosity is the occurrence of a lithosphere or layer of low-temperature, high-viscosity fluid in the uppermost coldest part of the top cold thermal boundary layer (e.g. Parmentier & Turcotte 1978; Christensen 1984*b*). Of course, it is beyond the scope of two-dimensional numerical simulations to address the problem of how the strong temperature-dependence of viscosity modifies the three-dimensional flow pattern of mantle convection.

Three-dimensional convection of fluids with temperature-dependent viscosity has been studied by laboratory experiments (e.g. Richter 1978; White 1988). These investigations have identified roll and bimodal patterns of convection for fluids with mildly temperature-dependent viscosity and hexagonal, square, and spoke patterns of convection with hot upwelling cylindrical plumes and cold downwelling sheets for fluids with strongly temperature-dependent viscosity. However, in laboratory experiments, it is difficult to examine these three-dimensional flow patterns in detail. Numerical experiments facilitate such detailed examinations of complex three-dimensional convective flow patterns.

Three-dimensional numerical calculations have been carried out for thermal convection of a constant viscosity fluid in a rectangular box (Cserepes, Rabinowicz & Rosemberg-Borot 1988; Houseman 1988; Travis, Olson & Schubert 1990*a*; Travis, Weinstein & Olson 1990*b*) and in a spherical shell (Baumgardner 1985; Zebib, Goyal & Schubert 1985; Machetel, Rabinowicz & Bernardet 1986; Glatzmaier 1988; Bercovici, Schubert & Glatzmaier 1989*a*, *b*; Bercovici *et al.* 1989*c*) as well as for thermal convection of a mildly temperature-dependent viscosity fluid in a rectangular box (up to 10^2 in the ratio of largest to smallest viscosity) (Christensen & Harder 1991). These studies have identified the main features of three-dimensional convection to be cylindrical-like upwelling plumes and sheet-like downwelling structures. No one, however, has succeeded in calculating thermal convection of a strongly temperature-dependent viscosity fluid with the ratio of largest to smallest viscosity greater than 10^2. In this paper, we investigate how a strong variation of viscosity with temperature, up to a factor of 10^5 in the ratio of largest to smallest viscosity, influences this style of three-dimensional convection.

2. Basic equations, numerical method, and model description

We consider the thermal convection of an infinite Prandtl number fluid with a strongly temperature-dependent viscosity in a three-dimensional rectangular box heated from the bottom. The aspect ratios of the box a_x and a_y (width over height in the x- and y-directions, respectively) are assumed to be 1.7 and 0.5, respectively, in most of our calculations; the coordinate axes are parallel to the sides of the rectangular box with the z-axis vertical (positive upward) and the origin at a bottom corner of the box. We carried out a few calculations with the aspect ratios $a_x = 3$ and $a_y = 1.5$ to see how the flow pattern depends on aspect ratio. The non-dimensional forms of the energy, momentum, and continuity equations are, respectively,

$$\partial_t T + \boldsymbol{u}\cdot\boldsymbol{\nabla} T = \nabla^2 T, \tag{1}$$

$$-\nabla p + R_t T \boldsymbol{e}_z + \nabla \cdot [\eta(\nabla \boldsymbol{u} + {}^t\nabla \boldsymbol{u})] = 0, \tag{2}$$

$$\nabla \cdot \boldsymbol{u} = 0, \tag{3}$$

where superscript t means transpose, $\boldsymbol{u}$ is fluid velocity, p is pressure, T is temperature, η is viscosity (assumed to be a function of temperature), $\boldsymbol{e}_z$ is a vertical unit vector, and R_t is the Rayleigh number defined by

$$R_t = \alpha g h^3 \rho_0 \delta T / \eta_0 \kappa. \tag{4}$$

In (4), ρ_0 is the density at $T = 0$, η_0 is a dimensional reference viscosity, g is the acceleration due to gravity, κ is thermal diffusivity, h is the height of the box, δT is the temperature difference between the top and bottom surfaces of the box (see below for the thermal boundary conditions at the top and bottom), and α is thermal expansivity. All quantities on the right-hand side of (4) are dimensional. In (1)–(3), length is normalized with h, temperature is normalized with δT, and time is normalized with the thermal diffusion time h^2/κ. Non-dimensional viscosity η is assumed to depend on T as

$$\eta = \exp(-ET), \tag{5}$$

where E is a constant. The reference dimensional viscosity η_0 is taken to be the viscosity at $T = 0$.

The boundary conditions at the vertical sidewalls are assumed to be reflection conditions

$$\boldsymbol{n} \cdot \nabla \boldsymbol{u}_t = 0, \tag{6}$$

$$\boldsymbol{n} \cdot \boldsymbol{u} = 0, \tag{7}$$

$$\boldsymbol{n} \cdot \nabla T = 0, \tag{8}$$

where $\boldsymbol{n}$ is the normal vector and $\boldsymbol{u}_t$ is the tangential component of fluid velocity. The top ($z = 1$) and bottom ($z = 0$) boundaries are isothermal surfaces

$$T = 0 \quad \text{at } z = 1, \tag{9}$$

$$T = 1 \quad \text{at } z = 0. \tag{10}$$

The top and bottom surfaces are also impermeable and shear stress free

$$\boldsymbol{n} \cdot \boldsymbol{u} = 0 \quad \text{at } z = 0, 1, \tag{11}$$

$$\partial_z \boldsymbol{u}_t = 0 \quad \text{at } z = 0, 1. \tag{12}$$

In the following, we discuss the results in terms of R_t defined by (4) and r defined by

$$r = \exp(E). \tag{13}$$

The Rayleigh number R_t is defined with the viscosity at the top boundary where $T = 0$ and r is the viscosity ratio between the top and bottom boundaries ($T = 1$ at the bottom surface). It will also be convenient to introduce R_b, the Rayleigh number based on the viscosity at the temperature of the bottom boundary

$$R_b = r R_t. \tag{14}$$

The basic equations (1)–(3) are discretized using a backward finite-difference method in time and a finite-volume method in space (Patankar 1980). The mesh is taken to be non-uniform with finer resolution near the boundaries to resolve thermal boundary layers and plumes; mesh intervals vary in a geometric ratio with the ratio 1.06 in the x- and y-directions and 1.07 in the z-direction. The minimum mesh intervals $(\delta x, \delta y, \delta z)_{\min}$ and the number of mesh points (m_x, m_y, m_z) are given in table

Case	R_t	R_b	r	IC	Mode of calculation	Nu
			$a_x = 1.7, \quad a_y = 0.5$			
			$(m_x, m_y, m_z) = (24, 14, 22), \quad (\delta x, \delta y, \delta z)_{\min} = (5, 3, 3.2) \times 10^{-2}$			
1	10^5	10^5	1	hyd	std	9.72
2	3.2×10^4	10^5	3.2	1	std	7.41
3	10^4	10^5	10	2	std	6.26
4	10^3	10^5	10^2	3	std	4.13
5	3.2×10^2	10^5	3.2×10^2	4	std	3.08
6	32	10^5	3.2×10^3	5	std	1.54
7	32	10^5	3.2×10^3	10	std	1.54
8	10^3	3.2×10^5	3.2×10^2	4	std	4.47
9	10^3	3.2×10^5	3.2×10^2	10	std	4.47
10	10^3	10^6	10^3	8	std	4.96
11	10^3	10^6	10^3	10	tm	4.96
12	3.2×10^2	1.5×10^6	4.7×10^3	5	std	3.88
13	3.2×10^2	1.5×10^6	4.7×10^3	rnd	std	3.77
			$(m_x, m_y, m_z) = (24, 14, 24), \quad (\delta x, \delta y, \delta z)_{\min} = (5, 3, 2.1) \times 10^{-2}$			
14	10^3	3.2×10^6	3.2×10^3	10	tm	5.47
			$(m_x, m_y, m_z) = (44, 18, 30), \quad (\delta x, \delta y, \delta z)_{\min} = (1.7, 2.1, 1.7) \times 10^{-2}$			
15	10^3	5×10^6	5×10^3	14	std	5.55
16	10^3	3.2×10^6	3.2×10^3	14	std	5.37
			$(m_x, m_y, m_z) = (44, 18, 30), \quad (\delta x, \delta y, \delta z)_{\min} = (1.7, 2.1, 1.3) \times 10^{-2}$			
17	10^2	3.2×10^6	3.2×10^4	16	std	3.61
18	32	3.2×10^6	10^5	17	std	3.17
19	32	10^6	3.2×10^4	18	std	2.56
20	10	3.2×10^5	3.2×10^4	19	std	1.78
21	3.2×10^2	3.2×10^6	10^4	17	std	4.31
22	3.2×10^2	3.2×10^6	10^4	12	std	4.05
			$a_x = 3, \quad a_y = 1.5$			
			$(m_x, m_y, m_z) = (68, 30, 22), \quad (\delta x, \delta y, \delta z)_{\min} = (3.5, 3.5, 3.2) \times 10^{-2}$			
23	10^3	10^6	10^3	hx	std	4.95
24	32	10^6	3.2×10^4	23	std	2.59

TABLE 1. Input parameter values and values of the Nusselt number. IC means initial conditions, hyd refers to the state given by (15) and (16), rnd refers to the state given by (15) and temperature perturbations in the form of random noise, hx indicates the hexagonal pattern shown in figure 14, and std and tm indicate steady state and time marching calculations, respectively. The numbers under the IC column refer to the case adopted as the initial state.

1. The discretized equations are solved by the SIMPLER algorithm (Patankar 1980); temperature T and the primitive variables p and $\boldsymbol{u}$ are treated as unknowns and iteratively determined line by line. Special care is taken in the calculation of viscosity to avoid possible numerical instabilities owing to the strong temperature-dependence of viscosity (see Appendix A). When the purpose is to obtain a steady state solution, the timestep is taken to be 10^{10} and time marching is done in only one step. Under-relaxation is employed with a relaxation constant of 0.1 for the momentum and continuity equations and a relaxation constant of 0.3 for the energy equation. The iteration procedure is concluded when the difference between the horizontally averaged heat flow between the top and bottom boundaries becomes smaller than

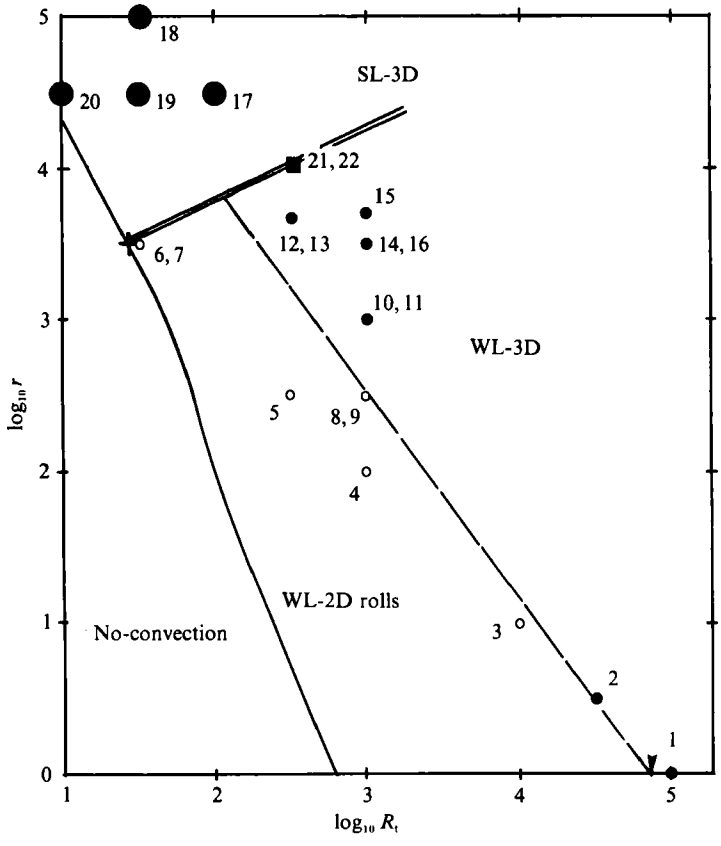

FIGURE 1. A regime diagram of convective flow patterns in the plane R_t (Rayleigh number defined with the viscosity at the top) *vs.* r (viscosity ratio between the top surface and the bottom boundary) for the case $a_x = 1.7$ and $a_y = 0.5$. ●, Three-dimensional stagnant-lid mode of convection (SL-3D); •, three-dimensional whole-layer mode of convection (WL-3D); ○, two-dimensional whole-layer mode of convection (WL-2D rolls); ■, indicates that both stagnant-lid and whole-layer convection occur. The numbers attached to the circles refer to the case numbers in table 1. The dashed line and the double solid line show approximate boundaries between the convective regimes. ——, Critical Rayleigh number R_c as a function of r from the linear-stability analysis of Stengel *et al.* (1982). The arrow shows the location of the boundary between regimes WL-2D rolls and WL-3D at $r = 1$ calculated by Schnaubelt & Busse (1989). +, Location of the regime boundary between SL-3D and WL-2D on the solid line suggested by Stengel *et al.* (1982).

0.02%; 300–2000 iterations were necessary to satisfy this condition. When the purpose is to obtain a time-dependent solution, the timestep is taken to be less than one-third of the Courant condition. The reliability of the numerical code is verified by benchmark tests described in Appendix B.

3. Results

The set of calculations discussed here is summarized in table 1 which gives a_x, a_y, R_t, R_b, r, $(\delta x, \delta y, \delta z)_{\min}$, (m_x, m_y, m_z), the mode of solution (time marching tm or steady state std), the initial conditions (IC), and the computed values of Nusselt number Nu. The numbers under the initial condition column identify the case

adopted as the initial state for the calculation. The 'hyd' in the initial condition column for case 1 refers to the hydrostatic and conductive state

$$T = 1-z, \quad \boldsymbol{u} = 0, \tag{15}$$

and a temperature perturbation T' of the form

$$T' = 0.01 \cos(\pi x/a_x) \sin(\pi z). \tag{16}$$

The 'rnd' for case 13 in the initial condition column refers to the hydrostatic and conductive state (15) together with a temperature perturbation in the form of random noise with amplitudes in a range from 0 to 0.01. The 'hx' for case 23 in the initial condition column refers to the hexagonal pattern shown in figure 14.

The regime diagram of figure 1 ($\log_{10} r$ *vs.* $\log_{10} R_t$) classifies the convective flow patterns obtained in the cases with $a_x = 1.7$ and $a_y = 0.5$ into a steady 'stagnant-lid mode' (SL) indicated by large solid circles and a steady 'whole-layer mode' (WL) indicated by small circles. (We have not calculated time-dependent solutions.) The solid square in figure 1 indicates that both the whole-layer mode and the stagnant-lid mode of convection are obtained. The whole-layer mode of convective solutions is further classified into two-dimensional rolls (small open circles) and three-dimensional convection (small solid circles). (The stagnant-lid mode of convection was always found to be three-dimensional.) Schnaubelt & Busse (1989) showed that steady two-dimensional rolls with $r = 1$ and aspect ratio 1.7 (the aspect ratio adopted in our numerical simulations of two-dimensional roll pattern convection, see §3.3 below) are stable only when $R_t < 8.1 \times 10^4$. This threshold is shown by an arrow in figure 1. We also show, by a solid line, the critical Rayleigh number R_c as a function of r from the linear stability analysis of Stengel, Oliver & Booker (1982). This line gives an approximate location of the threshold for the onset of convection; it does not show the exact location because (*a*) the adopted width of the box is different from the critical wavelength and (*b*) the hydrostatic and conduction state is unstable against finite-amplitude perturbations at a value of R_t slightly smaller than R_c when η depends strongly on temperature (Busse 1967; Stengel *et al.* 1982). A linear analysis of convective instability for the constant viscosity case (e.g. Chandrasekhar 1961) and figure 11 of Stengel *et al.* (1982) suggest, however, that the uncertainty deriving from these two reasons is unimportant on the scale of figure 1.

We draw an approximate regime boundary between the stagnant-lid mode of convection (SL-3D) and the whole-layer mode of convection by a double solid line. This line is determined from the cross and the solid square shown in figure 1; the cross indicates the location of the triple junction between the regimes of stagnant-lid mode, whole-layer mode and no-convection suggested in the linear-stability analysis of Stengel *et al.* (1982). We neglected a flow regime along the double solid line, in which both stagnant-lid and whole-layer convection occur because this regime is likely to be narrow on the scale of figure 1 and our data points are not dense enough to resolve it. The equation for the regime boundary is

$$r = r_{c1} \equiv 1.18 \times 10^3 R_t^{0.309}. \tag{17}$$

We also draw the approximate regime boundary between the three-dimensional whole-layer mode of convection (WL-3D) and the two-dimensional whole-layer mode of convection (with aspect ratio 1.7, WL-2D Rolls) by a dashed line in figure 1. The equation of this boundary is

$$r = r_{c2} \equiv 3.84 \times 10^6 R_t^{-1.35}. \tag{18}$$

In the following, we describe the convective flow patterns obtained in each of these regimes. (We have neglected a possible regime of three-dimensional convection at R_t slightly greater than R_c in figure 1. Bolton & Busse (1985) have shown that convection becomes two-dimensional at $r = 1$ and $a_x = 1.7$ when R_t is larger than about 800, i.e. three-dimensional convection may occur when R_t is in a range from R_c (about 660) to 800 when $r = 1$. This range is small on the scale of figure 1.)

3.1. *Stagnant-lid mode versus whole-layer mode*

Figure 2 shows the structure of convection in case 17 ($R_t = 10^2$ and $r = 3.2 \times 10^4$, left column of figure) and case 16 ($R_t = 10^3$ and $r = 3.2 \times 10^3$, right column of figure); T_{av} and u_{av} in figure 2 (g) are defined by

$$T_{av} = \int dx \int dy\, T(x, y, z)/(a_x \times a_y) \tag{19}$$

and

$$u_{av} = u^*_{av}/u_{max}, \tag{20a}$$

where

$$u^*_{av} = \left[\int dx \int dy\, \boldsymbol{u}(x, y, z) \cdot \boldsymbol{u}(x, y, z)/(a_x \times a_y) \right]^{\frac{1}{2}} \tag{20b}$$

and u_{max} is the maximum value of u^*_{av}. In both equations, the integrations extend over the entire horizontal plane at height z. The viscosity η_{av} in figure 2 (g) is calculated from (5) and T_{av} and normalized with its value at the bottom. Note that $R_b = 3.2 \times 10^6$ for both cases.

Figure 2 for $r = 3.2 \times 10^4$ shows that a stagnant layer or lid develops in the uppermost coldest highly viscous part of the top cold thermal boundary layer when viscosity depends strongly on temperature; the average fluid velocity u_{av} is almost 0 at $z > 0.85$ (the height indicated by the arrow in figure 2g). Isotherms in the vertical sections in figure 2 (e, f) are almost horizontal and T_{av} depends linearly on z (figure 2g) in the stagnant lid, i.e. heat is transferred in the vertical direction only by conduction in the lid. Three-dimensional convection occurs beneath the stagnant lid. The convection has cylindrical hot uprising plumes and cylindrical cold sinking plumes (see figure 2a–d for $r = 3.2 \times 10^4$). The temperature contrast between the coldest part of the sinking plumes and the hottest part of the uprising plumes in the horizontal plane $z = 0.5$ is about 0.25 (figure 2d), much smaller than the temperature contrast between the top and bottom boundaries. We define this type of convection as the 'stagnant-lid' mode of convection. (Further discussion of the convective flow pattern of the stagnant-lid mode of convection will be given below.)

Figure 2 for $r = 3.2 \times 10^3$, in contrast, shows that convection involves all of the fluid in the box, including the fluid in the uppermost coldest highly viscous part of the top cold thermal boundary layer, when viscosity depends relatively mildly on temperature. The average fluid velocity u_{av} is non-zero (about 0.1) at the top boundary $z = 1$ as denoted by the arrow in figure 2 (g). The isotherms in the vertical sections in figures 2 (e) and 2(f) are significantly distorted from horizontal even just beneath the top boundary (note the $T = 0.1$ isotherm) and the dependence of T_{av} on z deviates significantly from linear in the top thermal boundary layer (figure 2g), i.e. advection significantly contributes to heat transport in the vertical direction even just beneath the top surface. As a result of the absence of a cold stagnant lid, the temperature contrast between the hottest parts of the uprising plumes and the coldest parts of sinking plumes is much larger than the corresponding temperature contrast for the case of stagnant-lid mode convection; the temperature contrast in the horizontal plane $z = 0.5$ is about 0.6, comparable to the temperature contrast

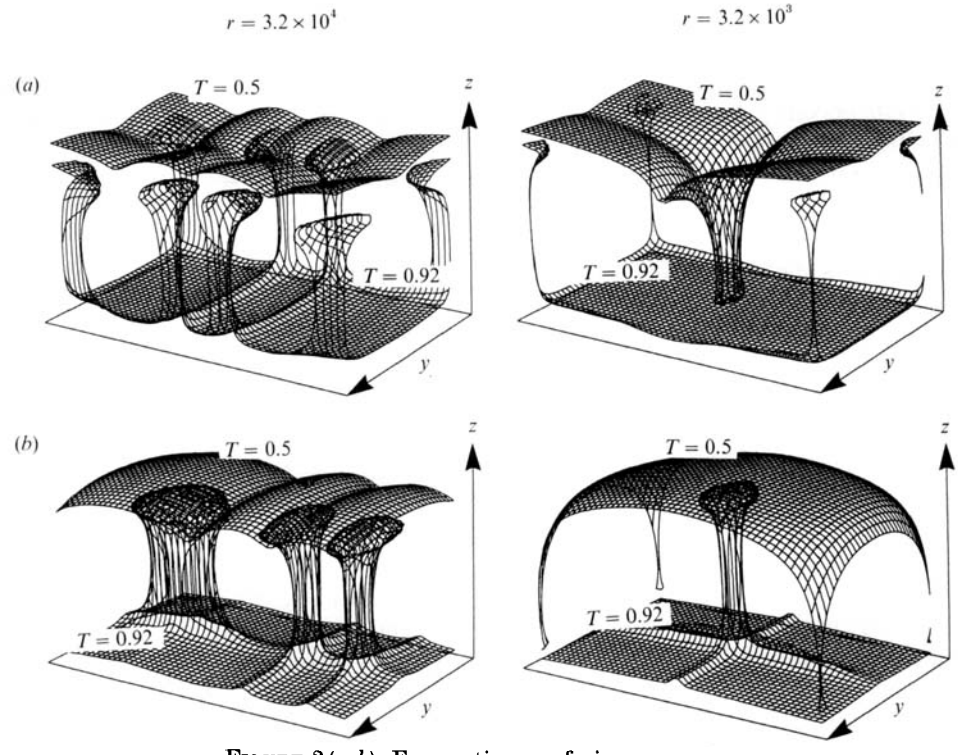

FIGURE 2(*a*, *b*). For caption see facing page.

between the top and bottom boundaries (see figure 2*d*). We define this type of convection as the 'whole-layer' mode of convection. (Further discussion of the flow pattern of the whole-layer mode of convection will be given below.)

To understand the nature of the transition between the stagnant-lid mode and the whole-layer mode, we plot the Nusselt number Nu and the horizontally averaged fluid velocity at the top $u_{\mathrm{av}}(z = 1)$ against $\log_{10} r$ at $R_{\mathrm{b}} = 3.2 \times 10^6$ in figure 3(*a*, *b*), respectively. The numbers attached to the data points indicate case numbers. The figures show that there is a hysteresis at $r = 10^4$. Case 21 is obtained when the stagnant-lid mode of convection calculated in case 17 is used as an initial guess in our iterative procedure. In contrast, case 22 is obtained when the whole-layer mode of convection calculated in case 12 is used as an initial guess. The hysteresis indicates that the transition between stagnant-lid and whole-layer convection is a bifurcation.

The slopes of the Nu versus r curves shown in figure 3(*a*) and the flow patterns shown in figure 3(*c*) also demonstrate that the transition between whole-layer and stagnant-lid convection is a bifurcation (figure 3*c* shows isotherms and contour lines of constant vertical fluid velocity in the horizontal plane at height $z = 0.5$). The Nusselt number Nu depends more strongly on r in the regime of whole-layer convection than in the regime of stagnant-lid convection and there is a qualitative difference in the flow pattern between the stagnant-lid mode of convection and the whole-layer mode of convection.

The bifurcation provides a physically sound basis for our classification of convection into whole-layer and stagnant-lid modes. The stagnant-lid and whole-layer modes belong to different branches of convection. The stagnant-lid mode of convection occurs when the viscosity ratio r exceeds r_{c1} defined in (17), while the

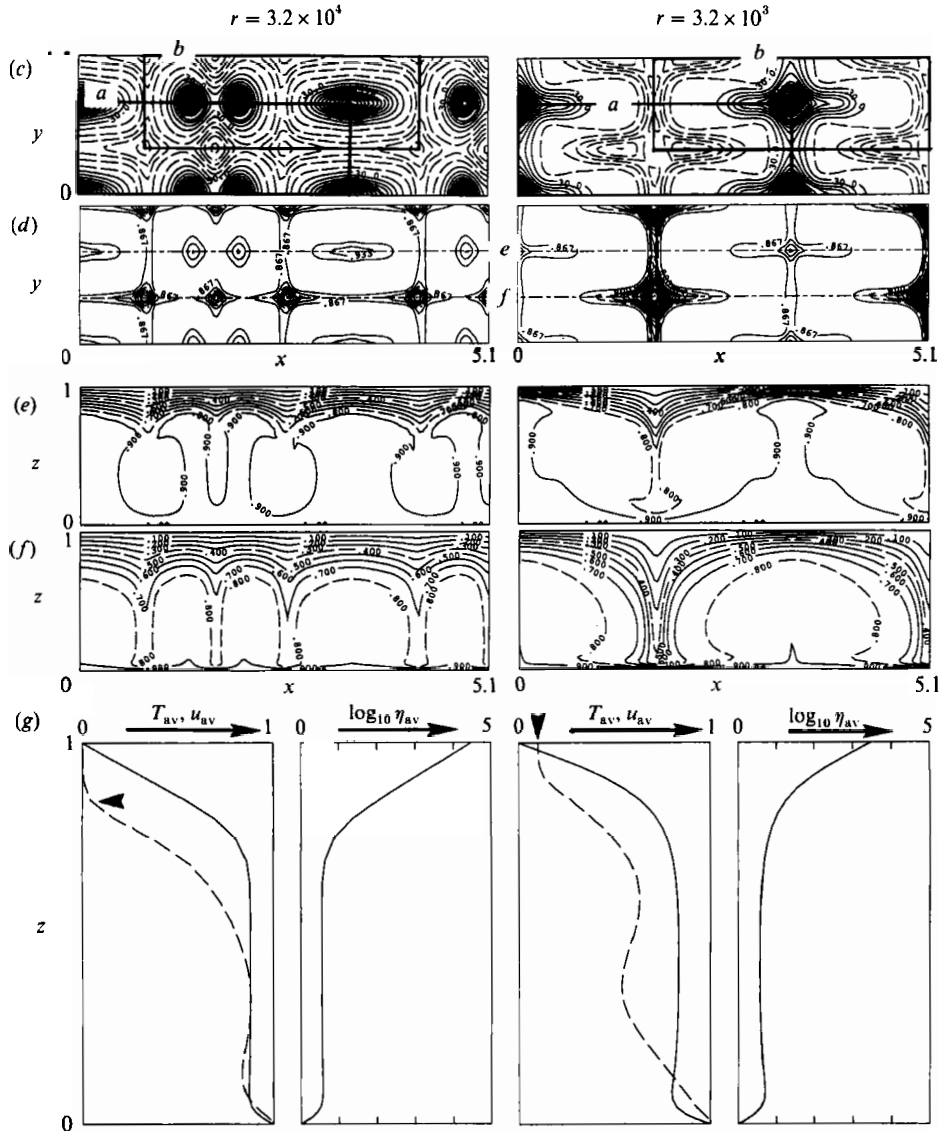

FIGURE 2. (*a*), (*b*) Isothermal surfaces in the areas of rectangles *a* and *b* shown in (*c*). (*c*) Contours of constant vertical velocity on the horizontal plane at height $z = 0.5$. Solid and dashed lines indicate upward and downward flow, respectively. Contour interval is 52.5. (*d*) Isotherms in the horizontal plane $z = 0.5$. Contour interval is 0.033. Dashed lines indicate the isotherms $T = 0.4$ and 0.8. (*e*), (*f*) Isotherms in the vertical sections at $y = 0.5$ and 1.0 indicated by the dash-dotted lines *e* and *f* shown in (*d*). Contour interval is 0.1. For dashed lines, see the caption to (*d*). (*g*) Horizontally averaged temperature T_{av} (solid line), horizontally averaged velocity u_{av} (dashed line, see (20)), and horizontally averaged viscosity η_{av} as a function of height *z*. The normalization constant u_{max} in (20*a*) is 230 (left-hand column) and 341 (right-hand column) and η_{av} is normalized with its value at the bottom. Parameter values are $r = 3.2 \times 10^4$, $R_t = 10^2$ (case 17, left-hand column) and $r = 3.2 \times 10^3$, $R_t = 10^3$ (case 16, right-hand column); $R_b = 3.2 \times 10^6$, $a_x = 1.7$, and $a_y = 0.5$ for both cases. Actual calculations are made in the region $1.7 < x < 3.4$, $0.5 < y < 1.0$ and the calculated flow patterns are reflected with respect to the sidewalls to obtain figure 2(*c–f*).

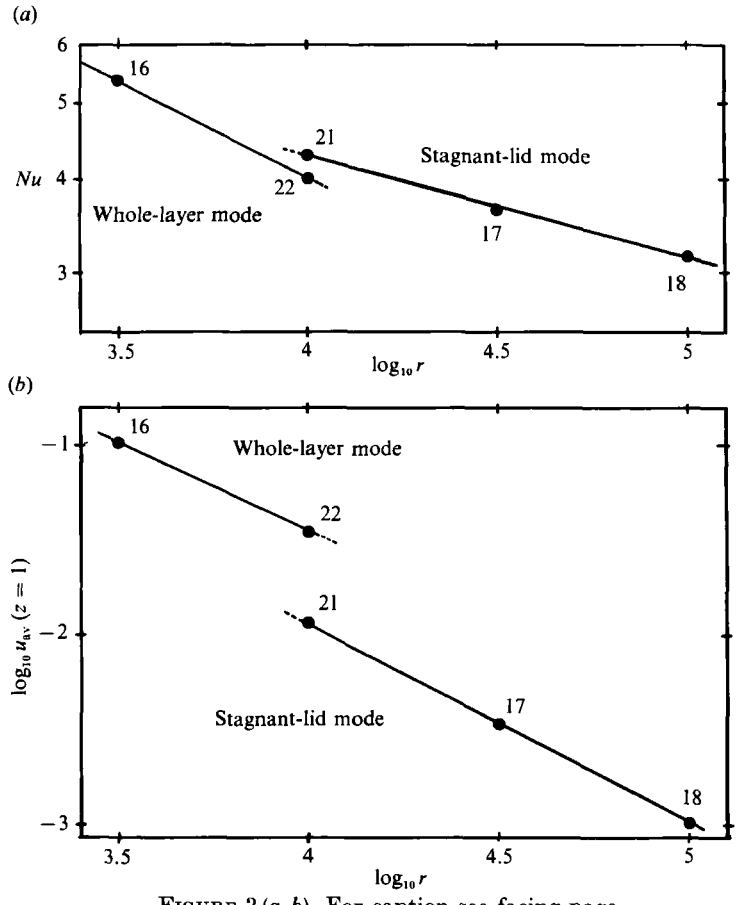

FIGURE 3(a, b). For caption see facing page.

whole-layer mode of convection occurs when r is smaller than r_{c1} as indicated in figure 1.

We confirmed the reliability of the above calculations by repeating the one at $r = 3.2 \times 10^3$ with a coarser mesh and with time marching (case 14, table 1). We obtained exactly the same structure of convection and a Nusselt number only 1.8% larger than the value obtained in the above calculation, as can be seen from table 1. We also confirmed that this solution is truely steady, i.e. it does not show time-dependence. Thus, we conclude that our calculation is reliable. (We also checked the effects of initial conditions on the numerical results. A discussion of this check is given below.)

In summary, a stagnant lid develops in the uppermost coldest highly viscous part of the top cold thermal boundary layer and convection is confined to the region beneath the stagnant lid only when the viscosity contrast r exceeds r_{c1}. When r is less than r_{c1}, convection penetrates upward into the highly viscous part of the top cold thermal boundary layer. The transition at r_{c1} is a bifurcation.

3.2. *Stagnant-lid convection mode*

Figure 4 shows the convective flow patterns obtained at $r = 3.2 \times 10^4$ and $R_t = 10$ and 32 (i.e. in the SL-3D regime of figure 1). This figure and figure 2 for $r = 3.2 \times 10^4$ show that convection beneath the stagnant lid occurs in a rectangular pattern. The

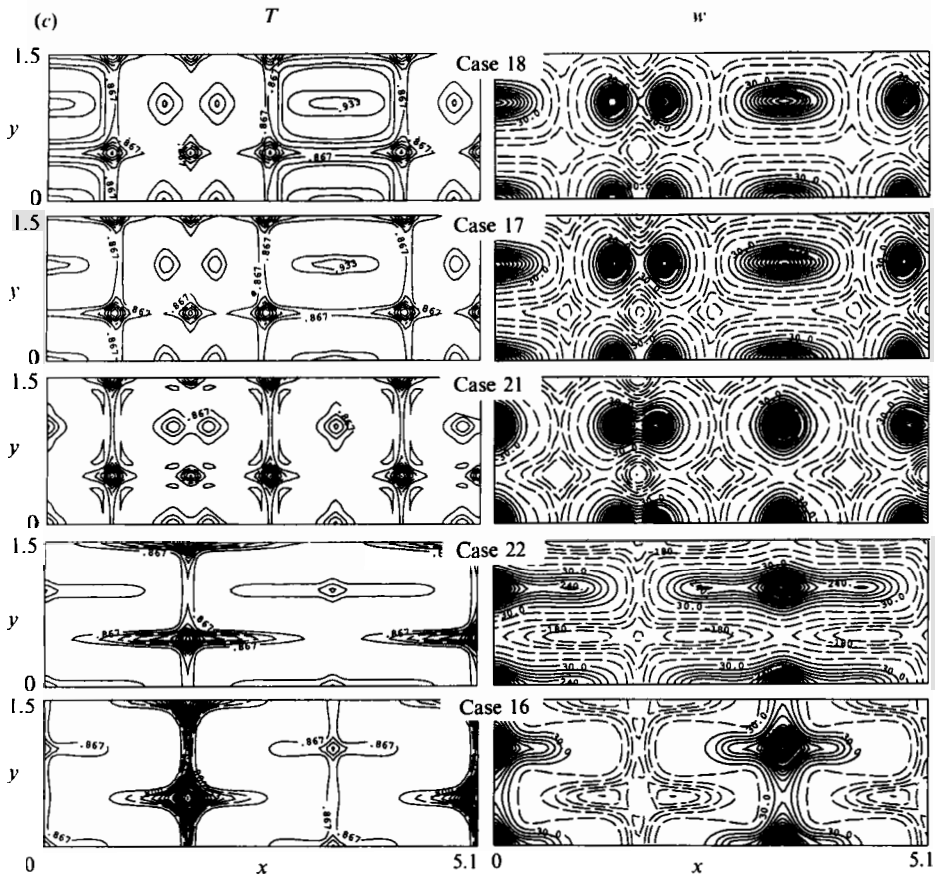

FIGURE 3. (*a*) Nusselt number Nu *vs.* $\log_{10} r$; r is the viscosity ratio across the convecting layer. The numbers attached to the points refer to the case numbers in table 1. All cases are calculated at the Rayleigh number defined with the viscosity at the bottom $R_b = 3.2 \times 10^6$. (*b*) Logarithm of horizontally averaged fluid velocity at the top $u_{av}(z = 1)$ *vs.* $\log_{10} r$; $u_{av}(z)$ is defined in (20). (*c*) Isotherms (left-hand column) and contour lines of constant vertical fluid velocity w (right-hand column) in the horizontal plane at the height $z = 0.5$ for the cases shown in (*a*) and (*b*). For contour intervals and the meaning of dashed lines, see the captions to figure 2(*c–d*).

planform of the rectangular three-dimensional convection has hot upwelling cylindrical plumes at or near the centre of the rectangle, sheets of cold sinking fluid along the four sides of the rectangle, and cold sinking cylindrical plume concentrations immersed in the sheets.

To see how the aspect ratios of the box influence the flow pattern of stagnant-lid convection, we repeated the calculation at $R_t = 32$ and $r = 3.2 \times 10^4$ with the aspect ratios $a_x = 3$ and $a_y = 1.5$ (case 24). Figure 5 shows the result. Figure 5(*g*) demonstrates that in this case convection is of the stagnant-lid type; fluid velocity is almost zero above the level shown by the arrow. Figure 5(*c–d*) indicates that convection in this case occurs in a rectangular pattern. The planform of the convection cells is rectangular with a hot upwelling plume at the centre of the rectangle, cold downwelling sheets along the four sides, and cold downwelling plume concentrations immersed in the sheets. These features are the same as those of the flow pattern shown in figure 4 for $R_t = 32$, i.e. the aspect ratios do not influence the overall character of the flow pattern. However, figure 4 for $R_t = 32$ and figure 5 show

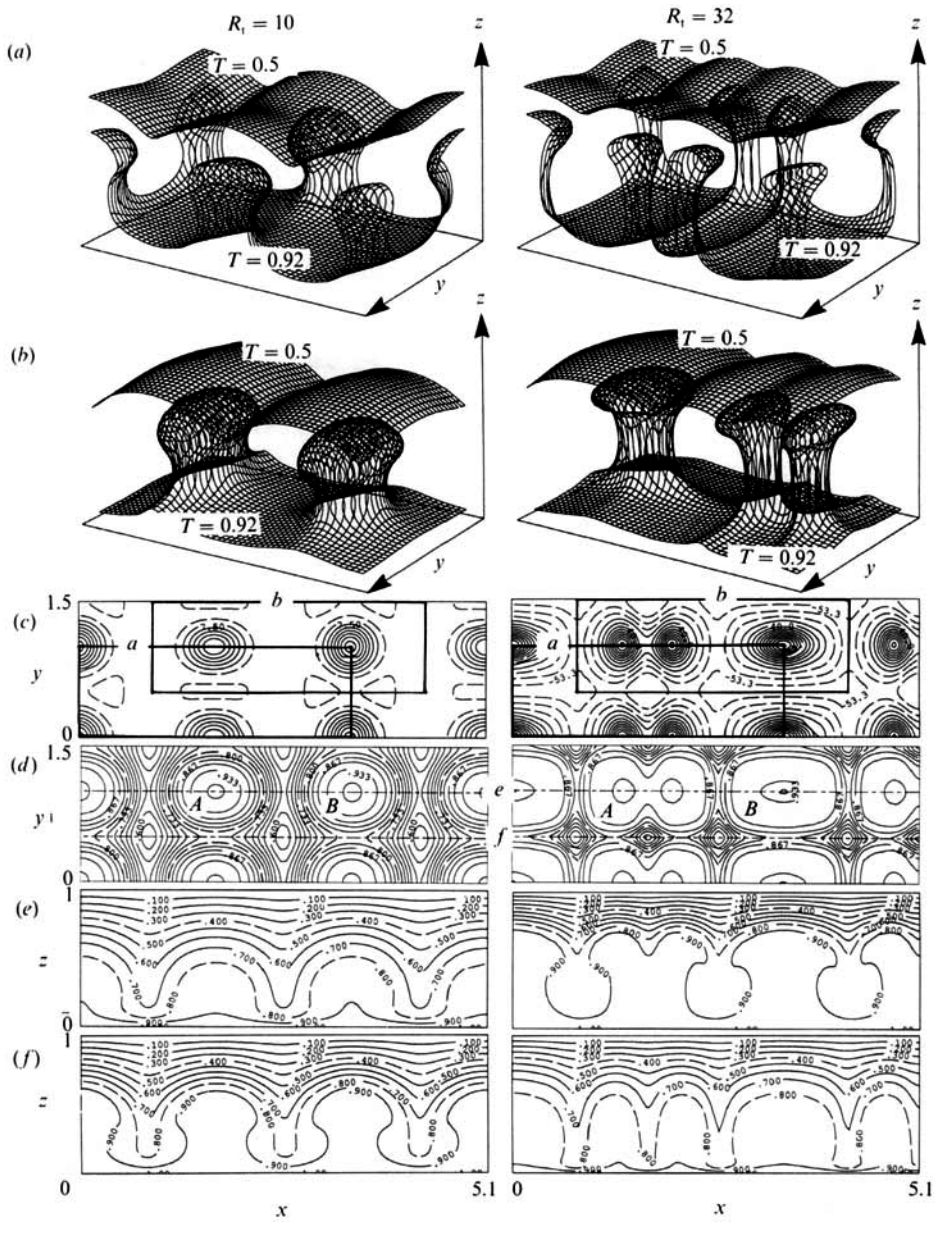

FIGURE 4. Similar to figure 2 (*a–f*) but for $R_t = 10$ (case 20, left-hand column) and $R_t = 32$ (case 19, right-hand column); r is 3.2×10^4 for both cases. The contour intervals for (*c*) are 8.13 (left) and 23.3 (right). The contour intervals for (*d*)–(*f*) are the same as those of figure 2.

that the detailed nature of the flow pattern does depend on the aspect ratios. All of the convection cells calculated at $a_x = 3$ and $a_y = 1.5$ have only one hot upwelling plume at their centres as shown in figure 5. In contrast, convection cell A in the calculation with $a_x = 1.7$ and $a_y = 0.5$ (figure 4*d*) has two upwelling plumes near the centre of the rectangle and six cold sinking plume concentrations, four at the corners and two on the sides of the rectangle, while the adjacent cell B has only one hot upwelling plume at the centre and four cold sinking plume concentrations at the corners of the rectangle (figure 4*b–d*).

3.3. *Whole-layer convection mode*

Figure 6 shows the structure of the whole-layer mode of convection at the values of r indicated in the figure. The Rayleigh number R_t is 10^3 for all cases. When $r = 320$, the convective flow pattern is a two-dimensional roll (WL-2D, figure 1) characterized by hot upwelling sheets around A and B (figure 6*d*) and a cold sinking sheet around F. The axis of the roll is parallel to the y-axis and the aspect ratio of the roll (width over depth) is equal to that of the convecting box $a_x = 1.7$. (This aspect ratio was always realized in our calculations of two-dimensional roll convection.) We obtained two-dimensional roll convection at $r = 3.2 \times 10^2$ and $R_t = 10^3$ even when a three-dimensional flow pattern was adopted for the initial state as indicated in table 1 and figure 1 (case 9). Thus we conclude that three-dimensional convection cannot occur in the WL-2D roll regime. (We carried out a similar check of the effect of initial conditions at $r = 3.2 \times 10^3$ and $R_t = 32$, i.e. case 7.)

Convection occurs in a three-dimensional bimodal pattern when $r \geqslant 10^3$. The planform of the convection cell is rectangular and both the hottest parts of upwelling plumes, which occur at the four corners of the rectangle, and the coldest part of the sinking plume, which occurs at the centre of the rectangle, are cylindrical. The cylindrical concentrations of the plumes become narrower as r increases, i.e. as the dependence of viscosity on temperature becomes stronger. The vertical velocities in the cylindrical cores of the hot upwelling plumes are much larger than the upwelling velocities in the surrounding fluid, while the vertical velocity in the cylindrical core of the cold sinking plume is almost the same as the downwelling velocity in the surrounding fluid. (Here, 'surrounding fluid' means the fluid in the sheet-like extensions of the plumes as explained below.) The rather low vertical velocity in the cylindrical core of the cold sinking plume is due to the high viscosity in the cold downwelling concentration.

In addition to the cylindrical cores, all of the plumes shown in figure 6 for $r \geqslant 10^3$ have sheet-like extensions (see, for instance, the sheet-like extensions indicated by 'sh' in figure 6*b* for $r = 5 \times 10^3$ and in figure 6*d* for $r = 3.2 \times 10^3$). The sheet-like extensions of a cold sinking plume become narrower and more elongated as r increases and become the dominant feature of cold downwelling flow when $r \geqslant 3200$, as can be seen from figure 6*c*; the local maxima of downwelling velocity occur in the sheet-like extensions instead of in the cylindrical cores of cold sinking plumes when $r \geqslant 3200$. At $r = 5000$, the sheet-like extensions of the cold sinking plumes become so well developed that they even drag the hot buoyant fluid around G and H downward (figure 6*d*). The sheet-like extensions of the hot upwelling plumes also become more elongated as r increases, but they do not become narrower.

Sheet-like extensions of plumes are a feature of the bimodal convection of strongly temperature-dependent viscosity fluid as can be seen from a comparison of the convection patterns in figures 6 and 7; the latter figure shows the pattern of three-dimensional convection of a constant viscosity fluid at $R_t = 10^5$ (case 1). In this constant viscosity case, convection also occurs in a bimodal pattern, but the plumes do not have sheet-like extensions. Both hot upwelling flow and cold downwelling flow occur dominantly as cylindrical plumes. (Note the dense circular concentric contour lines of constant vertical fluid velocity around the plumes in figure 7*c*.)

To see how the aspect ratios of the box influence the flow pattern of the whole-layer mode of convection, we repeated the calculation at $R_t = 10^3$ and $r = 10^3$ with the aspect ratios $a_x = 3$ and $a_y = 1.5$ (case 23). Figure 8 shows the results. Figure 8(*g*) demonstrates that in this case convection is of the whole-layer type; the horizontally-

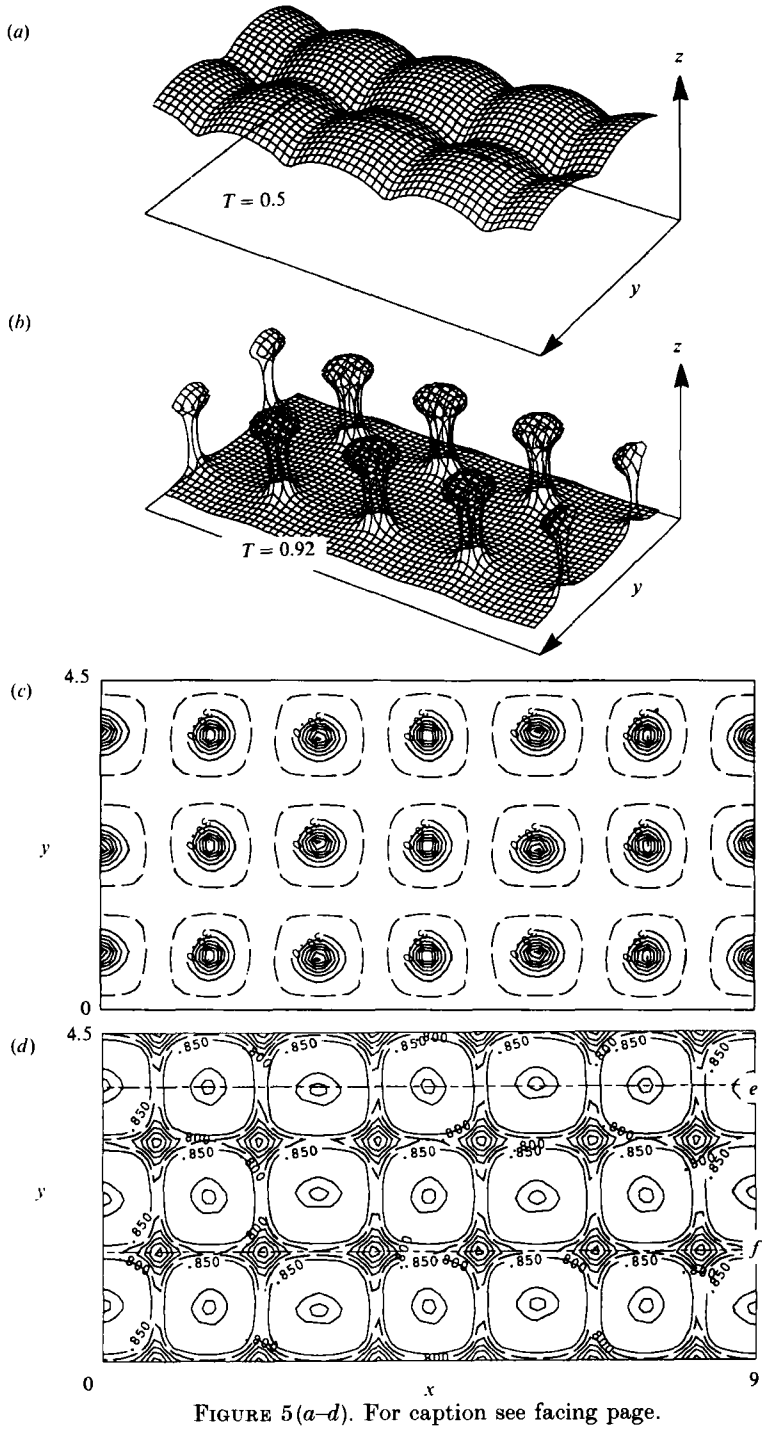

FIGURE 5(*a–d*). For caption see facing page.

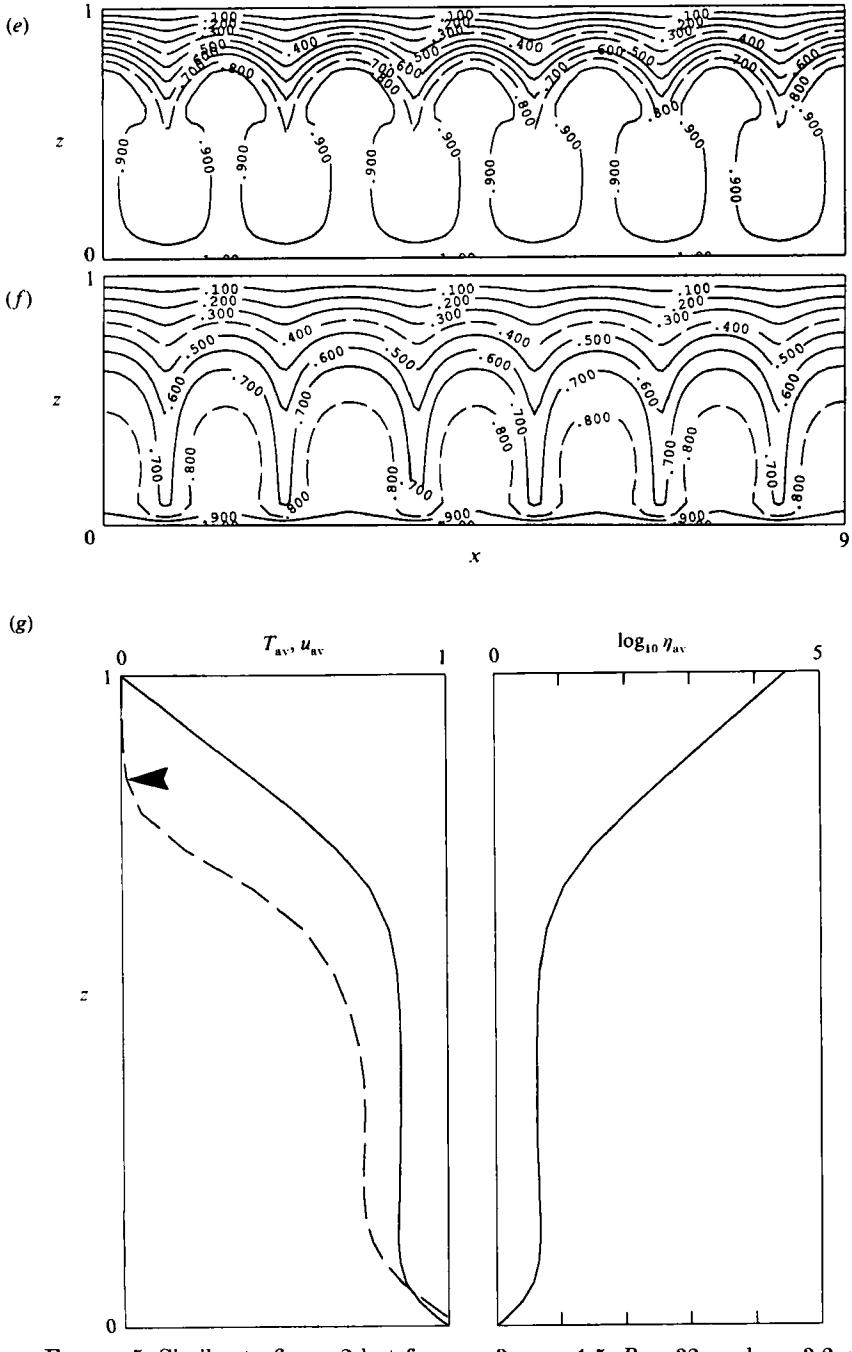

FIGURE 5. Similar to figure 2 but for $a_x = 3$, $a_y = 1.5$, $R_t = 32$, and $r = 3.2 \times 10^4$.

averaged fluid velocity u_{av} defined in (20) is non-zero (about 0.15) at the top boundary $z = 1$ as indicated by the arrow in the figure. Figure 8(*c–d*) indicates that in this case convection occurs in a bimodal pattern. The planform of convection is rectangular, with a hot upwelling plume at the centre of the cell and cold downwelling at the four corners of the cell. The plumes have sheet-like extensions.

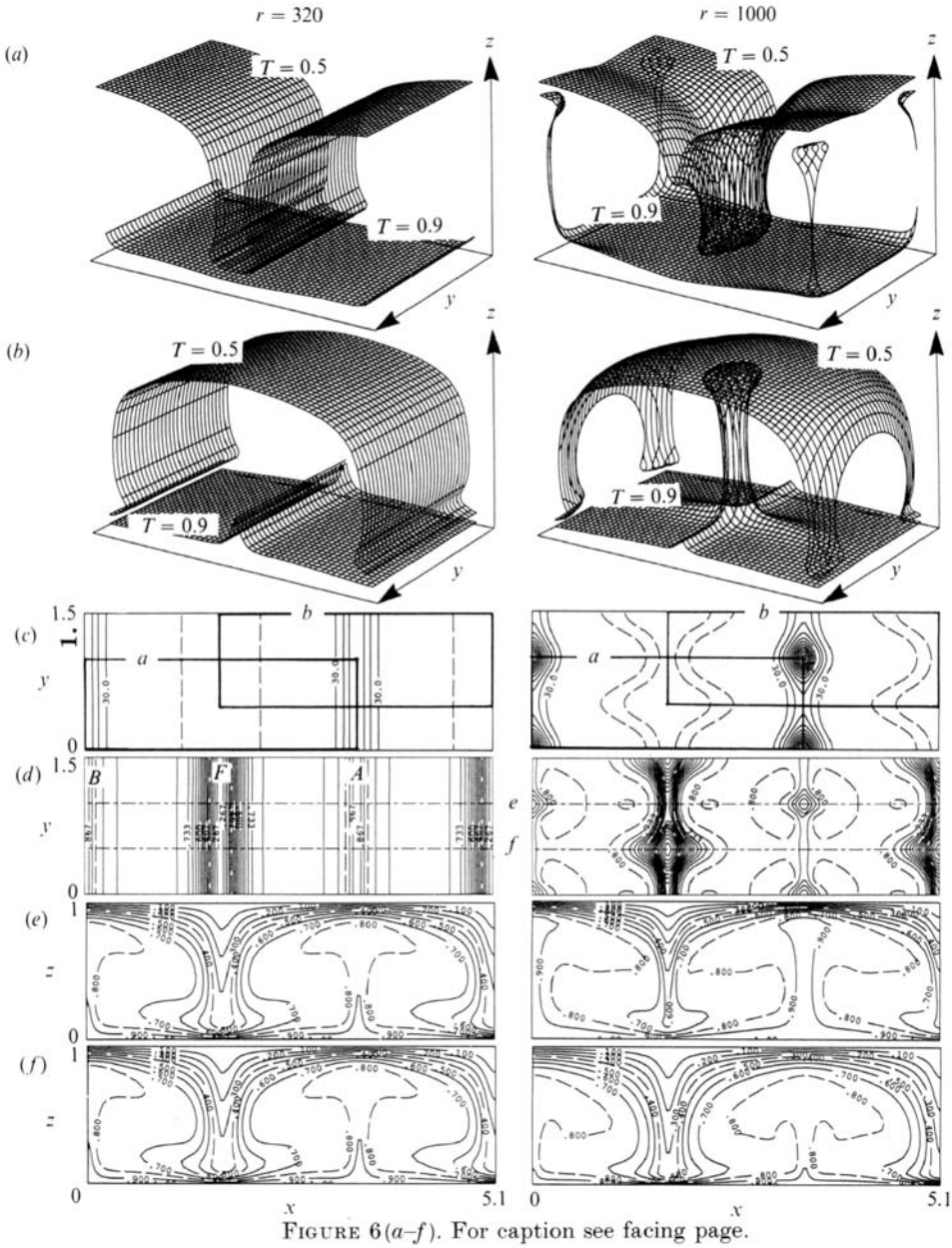

FIGURE 6(*a–f*). For caption see facing page.

The vertical velocity in the sheet-like extensions of the cold downwelling plumes is almost the same as the vertical velocity in the cylindrical cores of the plumes as can be seen from figure 8(*c*). These features are the same as the ones shown in figure 6 for $r = 10^3$, i.e. the aspect ratios of the box do not influence the overall character of the flow pattern. However, figure 8 shows that the detailed nature of the flow pattern does depend on the aspect ratios. Both hot upwelling plumes and cold downwelling plumes are not in a straight line. The locations of hot upwelling plumes deviate slightly from the dash–dotted line *e* in figure 8(*d*) and the locations of cold

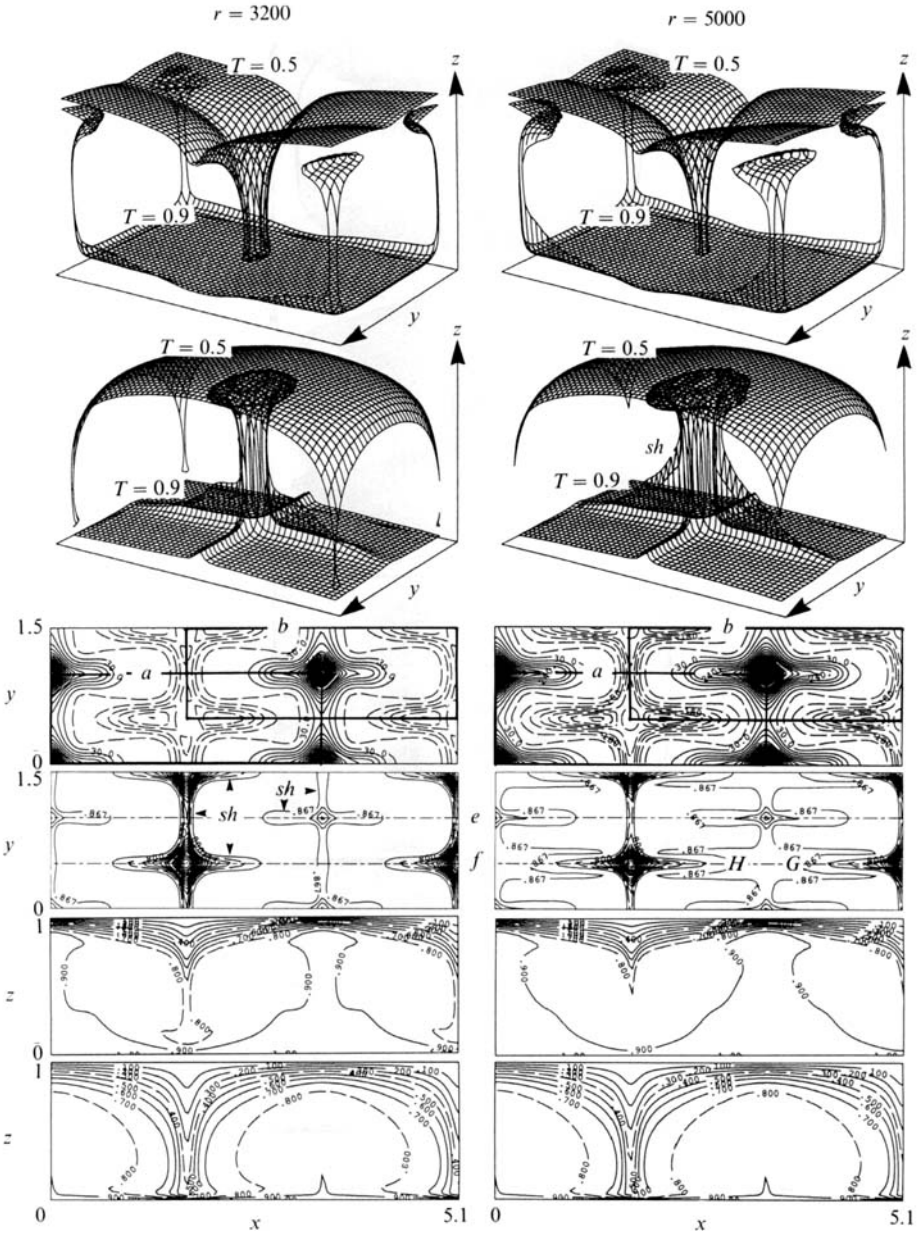

FIGURE 6. Similar to figure 2(*a–f*) but for $r = 320$ (case 8), 1000 (case 10), 3200 (case 16), and 5000 (case 15). The value of R_t is 10^3 for all cases.

downwelling plumes deviate slightly from the dash–dotted line *g*. These slight misalignments are not observed in the convection pattern of figure 6 for $r = 10^3$.

To confirm that our conclusion does not depend on assumed initial conditions, we made two numerical calculations with different initial conditions at $R_t = 3.2 \times 10^3$ and $r = 4.7 \times 10^3$. In one calculation (case 13), a hydrostatic and conductive state with random noise in the temperature distribution was assumed as the initial condition. We obtained convection cells having aspect ratio 1.7 in the x-direction and 1 in the y-direction and having the same structure as the one shown in figure 6 for

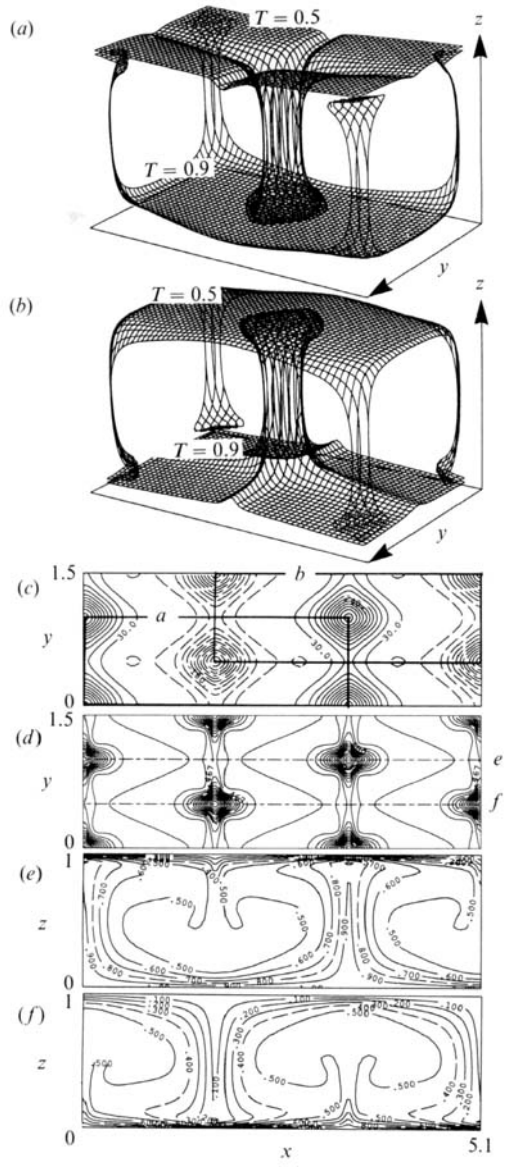

FIGURE 7. Similar to figure 2(*a–f*) but for a constant viscosity case at $R_t = 10^5$ (case 1).

$r = 10^3$. (This aspect ratio in the x-direction is half of the aspect ratio for the convection cell shown in figure 6 at $r = 10^3$.) In another calculation (case 12), the two-dimensional rolls obtained in case 5 (figure 1) were used as the initial condition. We obtained convection cells having aspect ratio 3.4 in the x-direction and 1 in the y-direction and having the same structure as the one shown in figure 6 for $r = 3.2 \times 10^3$. In both calculations, we obtained whole-layer bimodal convection with cylindrical plumes having sheet-like extensions. Thus we conclude that the above described convective structures are not a consequence of assumed initial conditions.

3.4. *Vertical component of vorticity*

Figure 9 shows the horizontally averaged magnitude of the vertical component of vorticity ω_z (solid curve) and the horizontally averaged magnitude of the horizontal component of vorticity ω_h (dashed curve) versus height z for (*a*) case 10 ($r = 10^3$, $R_t = 10^3$), (*b*) case 15 ($r = 5 \times 10^3$, $R_t = 10^3$), and (*c*) case 17 ($r = 3.2 \times 10^4$, $R_t = 10^2$). Here, ω_z and ω_h are defined by

$$\omega_z = \left[\int dx \int dy (\nabla \times \boldsymbol{u})_z^2 / (a_x a_y) \right]^{\frac{1}{2}}, \tag{21}$$

and

$$\omega_h = \left\{ \int dx \int dy \left[(\nabla \times \boldsymbol{u})_x^2 + (\nabla \times \boldsymbol{u})_y^2 \right] / (a_x a_y) \right\}^{\frac{1}{2}}, \tag{22}$$

where the integration extends over the entire horizontal plane at height z. The figure shows that ω_z, though non-zero, is much smaller than ω_h for all cases. The vertical component of vorticity, which in the case of mantle convection has a magnitude comparable to that of the horizontal component of vorticity at the Earth's surface, is not significantly excited in a thermally convecting Newtonian fluid with temperature-dependent viscosity even when the temperature-dependence is very strong. This result is consistent with the conclusion of Christensen & Harder (1991).

3.5. *Efficienty of heat transport*

Figure 10(*a*) shows Nusselt number Nu versus $\log_{10} R_t$ for the whole-layer mode of convection at $R_b = 10^5$. (Here, we present the results using R_t and R_b instead of R_t and r.) The values of Nu from cases 1–6 listed in table 1 are used in this plot. The figure shows that $\log_{10} Nu$ depends linearly on $\log_{10} R_t$ when $R_t > 100$. The large deviation from this relationship at $R_t = 32$ (case 6) occurs because this value of R_t is close to the threshold for convection to occur as can be seen from figure 1; the linear relationship is expected only when R_t is much higher than the critical Rayleigh number. By least-squares fitting to the data at $R_t > 100$, we obtain

$$Nu = 1.05 R_t^{0.192}, \tag{23}$$

when $R_b = 10^5$.

Figure 10(*b*) shows Nu versus $\log_{10} R_b$ for the whole-layer mode of convection at $R_t = 10^3$. The values of Nu from cases 8, 10, 15 and 16 as well as the value of Nu calculated from (23) at $R_t = 10^3$ are used in this plot. Again, there is a linear relationship between $\log_{10} Nu$ and $\log_{10} R_b$. By least-squares fitting, we obtain

$$Nu = 1.5 R_b^{0.086}, \tag{24}$$

when $R_t = 10^3$. The exponents in (23) and (24) indicate that the dependence of Nu on R_t (i.e. the viscosity at the top) is stronger than the dependence of Nu on R_b (i.e. the viscosity at the bottom) consistent with the two-dimensional results of Christensen (1984*a*).

Figure 3(*a*) shows Nu versus $\log_{10} R_t$ for the stagnant-lid mode at $R_b = 3.2 \times 10^6$. The points 21, 17 and 18 in the figure indicate that there is a linear relationship between $\log_{10} Nu$ and $\log_{10} R_t$. By least-squares fitting we obtain

$$Nu = 1.98 R_t^{0.133}, \tag{25}$$

when $R_b = 3.2 \times 10^6$. We have not derived a similar relation between Nu and R_b for the stagnant-lid mode of convection because we do not have enough data.

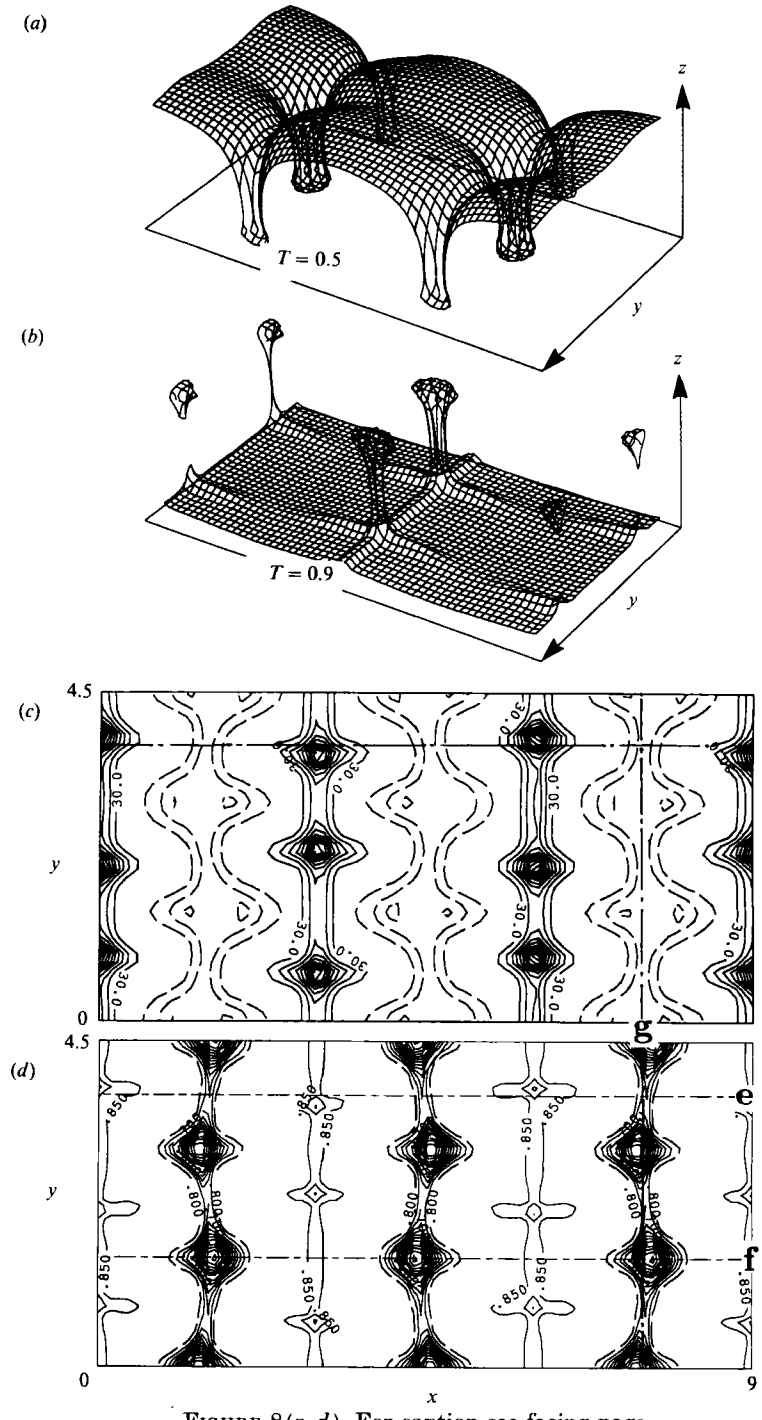

FIGURE 8(*a–d*). For caption see facing page.

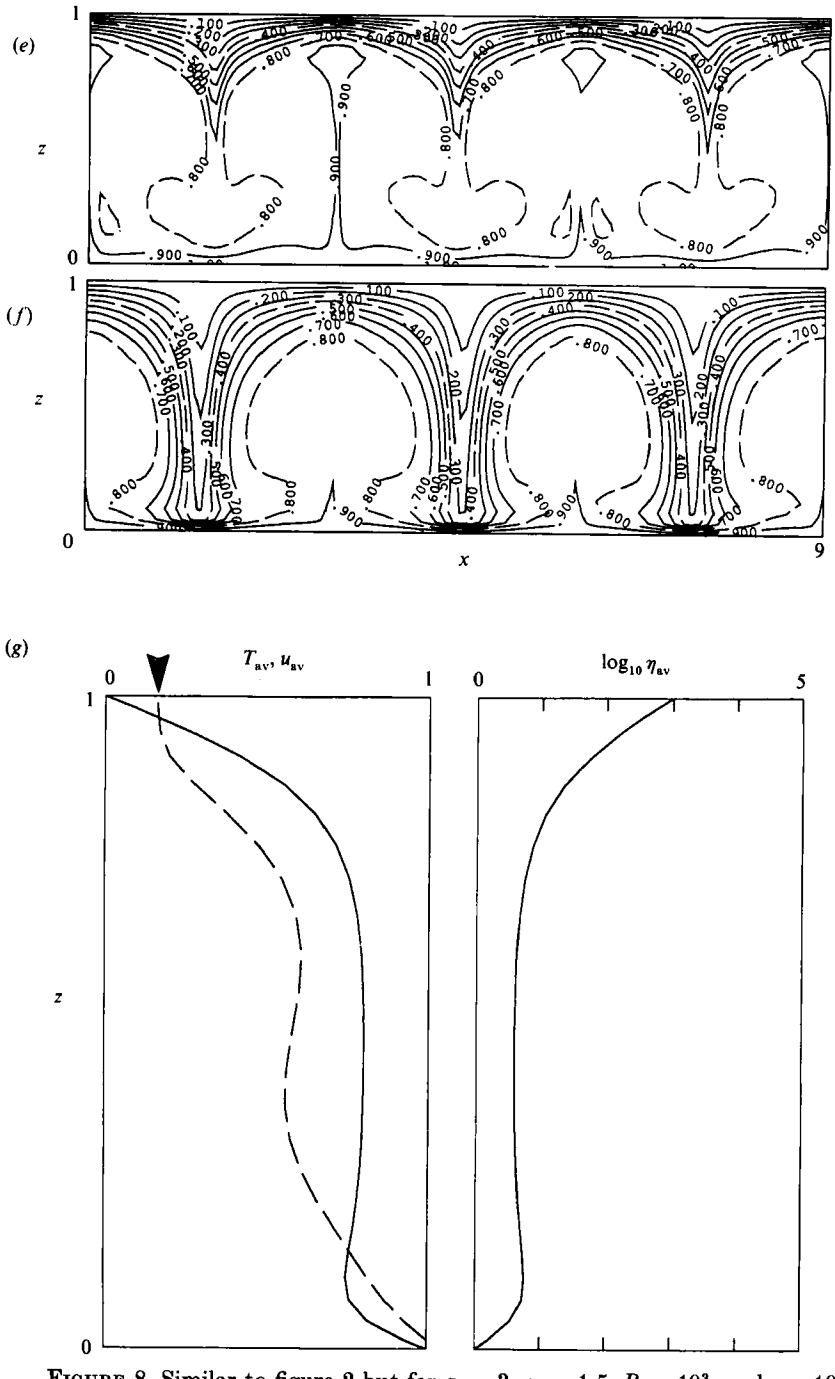

FIGURE 8. Similar to figure 2 but for $a_x = 3$, $a_y = 1.5$, $R_t = 10^3$, and $r = 10^3$.

3.6. *Summary*

The uppermost coldest highly viscous part of the top cold thermal boundary layer becomes a stagnant lid when the viscosity ratio $r > 1.18 \times 10^3 R_t^{0.309}$. Convection occurs in a three-dimensional rectangular pattern beneath this stagnant lid. A

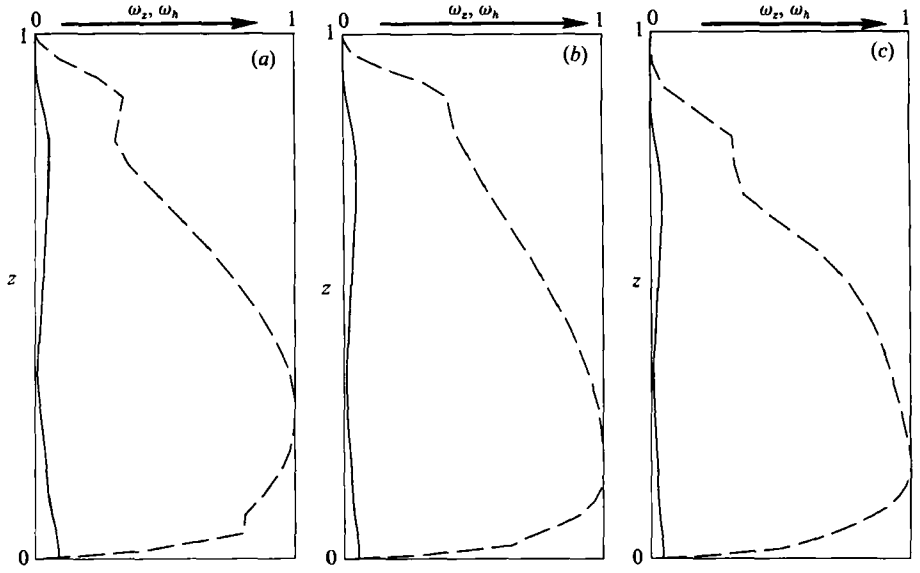

FIGURE 9. Horizontally averaged magnitude of the vertical vorticity component ω_z (solid line) and the horizontal vorticity component ω_h (dashed line) versus height z; both ω_h and ω_z are normalized with the maximum value of ω_h, which is (*a*) 979, (*b*) 2613, and (*c*) 2076. Parameter values are (*a*) $r = 10^3$, $R_t = 10^3$, (*b*) $r = 5 \times 10^3$, $R_t = 10^3$, and (*c*) $r = 3.2 \times 10^4$, $R_t = 10^2$.

stagnant lid does not develop when $r < 1.18 \times 10^3 R_t^{0.309}$; convection involves all of the fluid in the box including the fluid in the uppermost coldest highly viscous part of the top cold thermal boundary layer. This whole-layer mode of convection occurs in a three-dimensional bimodal pattern in regime 'WL-3D' shown in figure 1. The basically cylindrical plumes of this bimodal convection have sheet-like extensions, which become more well developed as the dependence of viscosity on temperature becomes stronger. The whole-layer mode of convection consists of two-dimensional rolls in the regime denoted by WL-2D rolls in figure 1. The transition between the whole-layer mode of convection and the stagnant-lid mode of convection is a bifurcation. Further detailed calculations are necessary to clarify the nature of this bifurcation. The Nusselt number Nu depends on R_t more strongly when convection occurs in the whole-layer mode than when it occurs in the stagnant-lid mode. The Nusselt number Nu for the whole-layer mode of convection depends more strongly on R_t than on R_b. The vertical component of vorticity is only slightly excited by the temperature-dependence of viscosity even when the dependence is very strong.

4. Discussion

The convective regime diagram of figure 1 may have implications for the tectonic evolution of terrestrial planets. The mantles of terrestrial planets have cooled by several hundred degrees over geologic time (e.g. Schubert, Cassen & Young 1979). Hence, mantle viscosity has increased by orders of magnitude at depth owing to the strong temperature-dependence of the viscosity of mantle material. The viscosity at the top of the mantle, however, has remained almost constant over geologic time because the surface temperature of terrestrial planets has been relatively unchanged. Thus, the viscosity contrast in the mantle has decreased by orders of magnitude with the age of the planets, while the Rayleigh number defined with respect to the

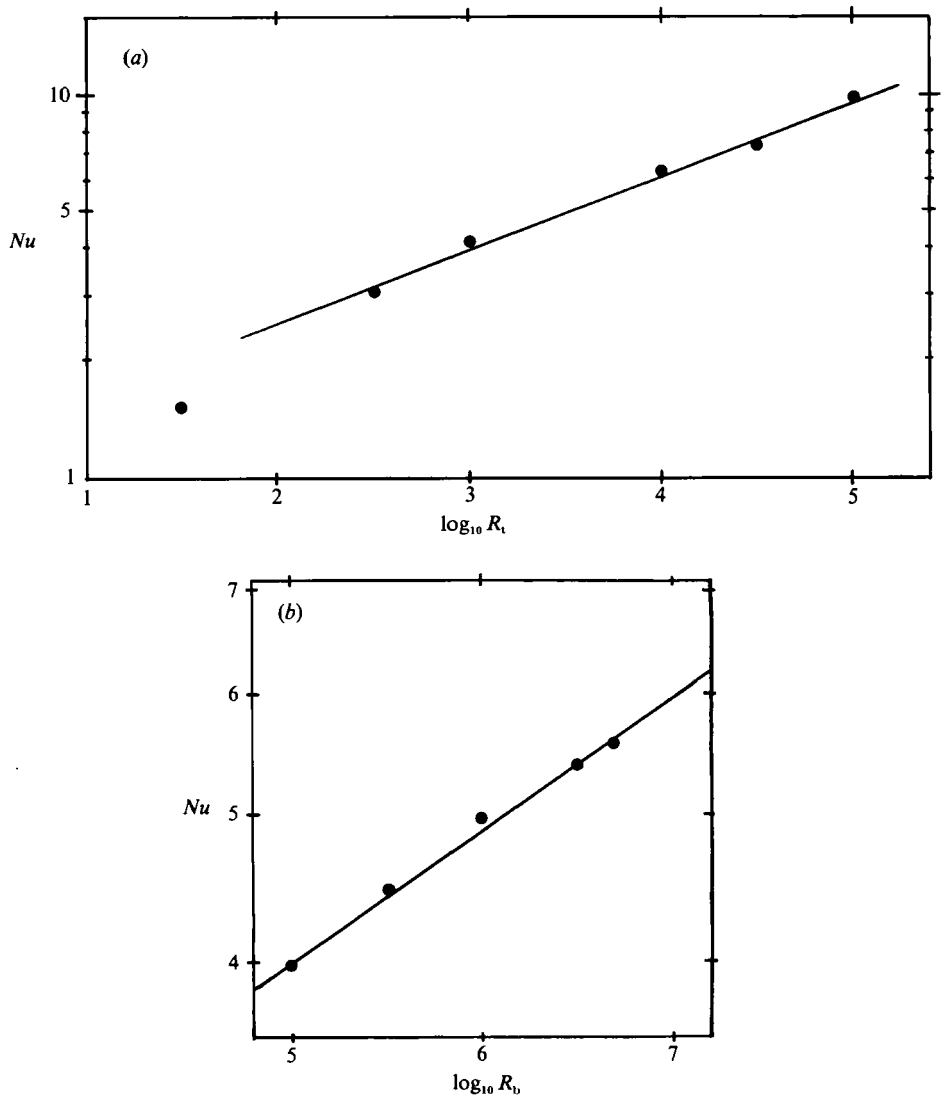

FIGURE 10. (*a*) *Nu vs.* $\log_{10} R_t$ for whole-layer mode of convection at $R_b = 10^5$. (*b*) *Nu vs.* $\log_{10} R_b$ for whole-layer mode of convection at $R_t = 10^3$. The value of *Nu* at $R_b = 10^5$ is calculated from (23).

viscosity at the top R_t has remained nearly constant. Therefore, the evolutionary paths of terrestrial planets are almost vertical in the regime diagram of figure 1.

The evolutionary path of a terrestrial planet may cross into the regime of whole-layer convection when R_t exceeds R_{tc}, the value of R_t for the cross in figure 1. Mantle convection would involve the lithosphere in a terrestrial planet with sufficiently large R_t when the viscosity contrast r becomes sufficiently small owing to the cooling of the planet. This is likely to be the case for the present Earth. The contrast between the effective viscosity of the Earth's lithosphere and underlying mantle is at most about three orders of magnitude (Kaula 1980) and R_t based on the effective viscosity of the lithosphere is much larger than R_{tc}. An evolutionary path that places the present Earth in the WL-3D regime of figure 1 is consistent with the occurrence of plate tectonics on the Earth; plate tectonics may thus be a particular manifestation of

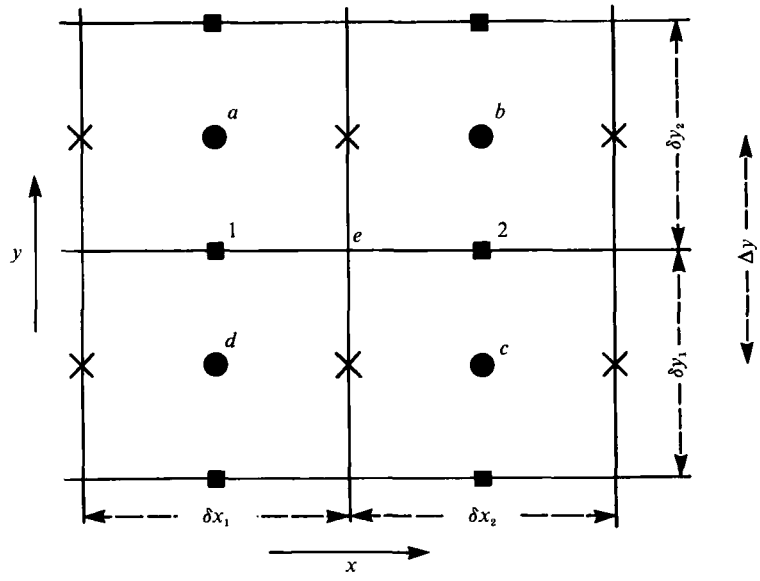

FIGURE 11. An illustration of the grid cell used in the present numerical experiments. Temperature, pressure, and viscosity are defined at the grid points a–d, the x-component of velocity is defined at the grid points denoted by crosses, and the y-component of velocity is defined at the grid points represented by solid squares.

WL-3D mode of convection. Venus may have followed a similar evolutionary path and the present Venus may have an even smaller viscosity contrast between its lithosphere and underlying mantle than does the Earth (Bindschadler, Schubert & Kaula 1990). The high surface temperature of Venus may preclude the expression of the involvement of the lithosphere in convection in the form of plate tectonics by suppressing the basalt–eclogite transition in the crust and hence by making the crust too buoyant to subduct (Anderson 1981).

The evolutionary path does not cross the regime of whole-layer convection for a terrestrial planet with R_t smaller than R_{tc}. The path crosses only the regimes of stagnant-lid and no-convection. Along this path, mantle convection occurs first beneath a stagnant lithosphere and then stops when r becomes sufficiently small owing to the cooling of the planet. It is possible that the Moon, Mercury and Mars may be following this evolutionary path although it is unlikely that at present they have crossed into the regime of no-convection. These bodies are smaller than the Earth and Venus and may have lithospheres with higher effective viscosities. Hence, R_t for these bodies is likely to be smaller than it is for the Earth and Venus.

We thank Bryan Travis of Los Alamos National Laboratory for providing us with his graphics code and the anonymous reviewers for useful comments.

Appendix A. Calculation of viscosity

In the finite-volume method (Patankar 1980), viscosity is defined at the centre of a grid cell and fluid velocity is defined on the boundaries between grid cells, as illustrated in figure 11. (Here, we explain the numerical method for the two-dimensional case for simplicity. Extension to the three-dimensional case is

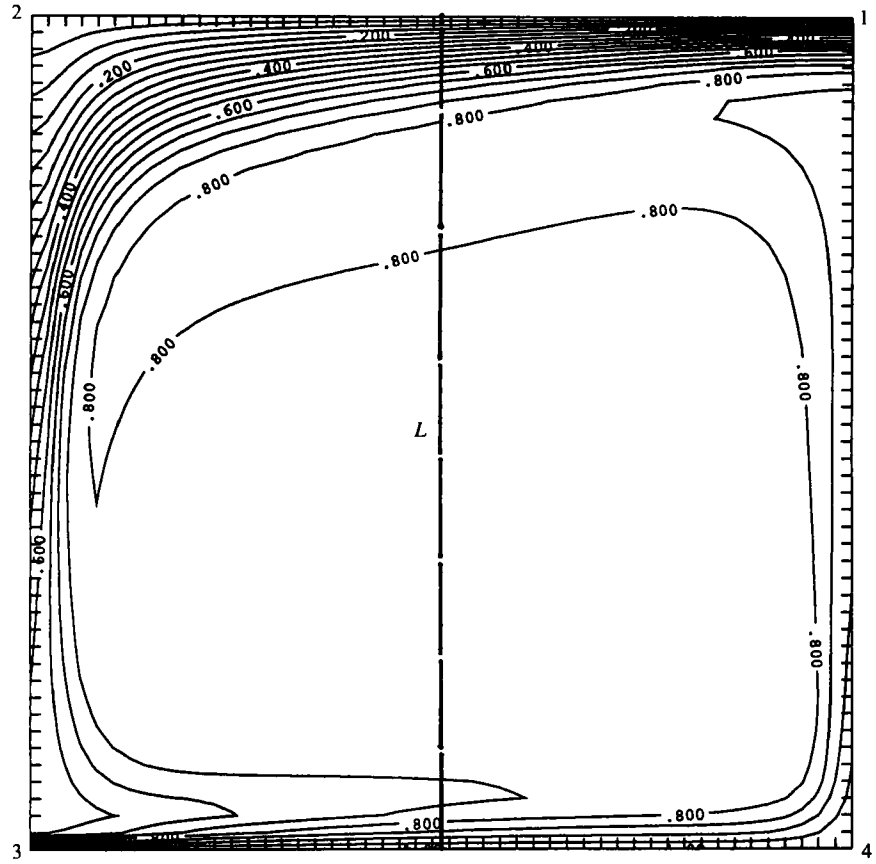

FIGURE 12. Isotherms for two-dimensional convection of a strongly temperature-dependent viscosity fluid obtained in a benchmark test of the code. Viscosity depends on temperature as in (5) and $R_t = 10^4$ and $R_b = 10^7$.

straightforward.) However, we need the values of viscosity at the corners of grid cells (e.g. point e in figure 1) when we calculate the viscous-drag term in the momentum equation. Special care is necessary in calculating this viscosity η_e from the values of viscosity at the neighbouring grid points by interpolation to avoid numerical instability. In the calculation of the x-momentum equation, for example, we calculate η_e from the following equation (Patankar 1980)

$$\eta_e = (\eta_1 \delta x_1 + \eta_2 \delta x_2)/(\delta x_1 + \delta x_2), \tag{A 1}$$

where

$$\eta_{1,2} = 2\Delta y/(\delta y_1/\eta_{d,c} + \delta y_2/\eta_{a,b}). \tag{A 2}$$

Here, η_i is the viscosity at point i in figure 11 and other quantities are defined in figure 11. Equation (A 1) is derived from the requirement that stress should be continuous across cell boundaries (Afrid 1990). When η_b, for example, is much larger than the viscosities at the points a, d and c, η_b contributes negligibly to the viscosity η_e. This is the basic property of the numerical approach that facilitates computation with large viscosity contrasts even between adjacent grid cells.

Quantity	Present result	Blankenbach *et al.* (1989)
Nu	10.097	10.066
v_{rms}	477.0	480.4
q_1	17.67	17.53
q_2	0.999	1.009
q_3	26.7	26.8
q_4	0.523	0.497
T_{c1}	0.736	0.741
z_{c1}	0.0622	0.0623
T_{c2}	0.829	0.832
z_{c2}	0.821	0.824
ξ_1	1015	1011
ξ_2	−4122	−4098
x_t	0.677	0.677
ξ_3	−804.5	−788.1
ξ_4	391.8	386.4
x_b	0.631	0.631

TABLE 2. Comparison of the present numerical results with the benchmark standard of Blankenbach *et al.* (1989). For the meaning of the symbols in the first column, see the text.

Appendix B. Benchmark tests of the numerical code

In order to test the validity of our numerical code, we compare our results with those of Blankenbach *et al.* (1989) for the cases of two-dimensional steady convection of a fluid with temperature-dependent viscosity in a bottom heated rectangular region of aspect ratio 1. Viscosity is assumed to depend on temperature as in (5). The boundary conditions are (6)–(12) and the Rayleigh numbers are $R_t = 10^4$ and $R_b = 10^7$. The convective flow pattern was forced to be two-dimensional by adopting a Hele-Shaw cell geometry for our rectangular box; the aspect ratios of the box a_x and a_y were assumed to be 1 and 0.1, respectively. (We also carried out the numerical simulation with $a_x = 0.1$ and $a_y = 1.0$.) The number of mesh points was $68(x-\text{direction}) \times 2(y-\text{direction}) \times 68(z-\text{direction})$ and the minimum mesh size was $\delta x_{\min} = \delta y_{\min} = 4.8 \times 10^{-3}$.

Figure 12 shows our calculated isotherms in the vertical plane $y = 0.05$. The single-cell, roll-like, counterclockwise convective circulation has thermal boundary layers at the top and bottom surfaces, plumes along the vertical sidewalls and an essentially isothermal core. The bottom thermal boundary layer is much thinner than the boundary layer at the top of the box. We calculated (*a*) Nusselt number Nu, (*b*) root-mean-square velocity defined by

$$v_{\mathrm{rms}}^2 = \int u^2 \, \mathrm{d}V/(a_x \times a_y), \tag{B 1}$$

where the volume integration extends over the entire box, (*c*) vertical temperature gradient at the four corners of the rectangle q_i ($i = 1$–4, figure 12), (*d*) the height z_e and the value T_e of the extremum of the temperature along the centre line $x = \frac{1}{2}$ (dashed line L in figure 12), (*e*) topography of the top and bottom free surfaces at the four corners of the box ξ_i measured in units of (m), and (*f*) the positions (x-coordinate) of the zero-crossings of the topography on the top and bottom free surfaces, x_t and x_b, respectively.

Case	a1	a2	a3	a4	a5	a6	a7
R_t	2410	2400	2000	1700	3000	3000	1800
r^*	11	11	11	11	4.5	6.0	11
v_{rms}	55.6	55.6	32.8	17.3	74.5	76.5	—
Nu (present)	1.73	1.71	1.51	1.33	1.85	1.86	—
Nu (BF)	1.69	1.67	1.48	1.30	—	—	1.36
Flow pattern							
Initial	R_5	SQ_3	ST	SQ_3	SQ_6	SQ_8	R_1
Final	R	SQ	SQ	SQ	R	SQ	(uR)
BF	sSQ	sSQ	sSQ	sSQ	uSQ	sSQ	sSQ
	sR	sR	uR	uR	sR	sR	uR

TABLE 3. Comparison of present numerical results with those of the weakly nonlinear analysis of Busse & Frick (1985) (denoted as BF) for three-dimensional convection of a mildly temperature-dependent viscosity fluid. The symbols ST, SQ and R mean static, square pattern convection, and roll pattern convection, respectively, and u and s in the last few rows mean unstable and stable respectively. The initial flow pattern of SQ_3 means the square pattern obtained in case a3. A time marching calculation was carried out in case a7. The (uR) for case a7 means roll pattern convection was found to be unstable but a final steady-state solution was not obtained in this calculation.

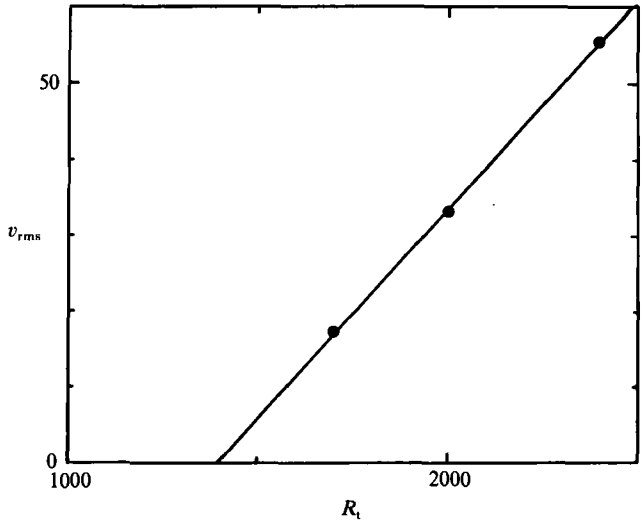

FIGURE 13. The relationship between root mean square velocity v_{rms} and Rayleigh number R_t for square pattern convection at $r^* = 11$. The data from cases a2, a3, and a4 in table 3 are plotted.

In addition to the summary of our results, table 2 includes results from the benchmark standard of Blankenbach *et al.* (1989). The agreement is satisfactory except perhaps for q_4, ξ_3 and ξ_4. The relative lack of agreement for these quantities occurs because the bottom thermal boundary layer is very thin, as can be seen from figure 12. A finer mesh is necessary to calculate these quantities more accurately. On the basis of table 2, we conclude that our numerical code accurately handles two-dimensional convection of strongly temperature-dependent viscosity fluid.

Next, we have carried out numerical simulations of the thermal convection of a mildly temperature-dependent viscosity fluid in a three-dimensional rectangular box and compared our results with those of a weakly nonlinear analysis by Busse & Frick (1985). The aspect ratios of the rectangular box are assumed to be $a_x = a_y = 1.0134$.

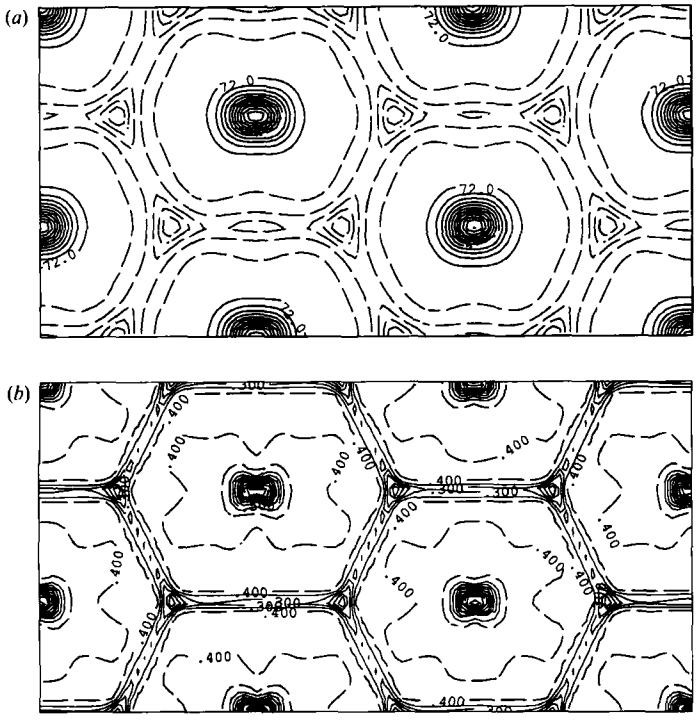

FIGURE 14. Contours of (*a*) constant vertical velocity and (*b*) isotherms in the horizontal plane $z = 0.5$ for hexagonal convection of a constant viscosity fluid in a box with aspect ratios $a_x = 3$ and $a_y = 1.5$. For the meaning of the dashed lines, see the caption to figure 2. Contour intervals are (*a*) 84 and (*b*) 0.125.

The problem involves the convection of fluid whose (non-dimensional) viscosity depends on temperature as

$$\eta = 1+2(1-r^*)(T-0.5)/(1+r^*), \qquad \text{(B 2)}$$

where r^* is the ratio of viscosity at the top, where $T = 0$, to the viscosity at the bottom, where $T = 1$. The reference dimensional viscosity η_0 in (4) is taken to be the viscosity at $T = 0.5$.

The assumed boundary conditions are (6)–(10) and zero fluid velocity at the top and bottom surfaces, i.e.

$$\boldsymbol{u} = 0 \quad \text{at } z = 0, 1. \qquad \text{(B3)}$$

The non-uniform mesh has $14 \times 14 \times 14$ mesh points. The minimum mesh size is $\delta x_{\min} = \delta y_{\min} = \delta z_{\min} = 0.061$, while the maximum mesh size is $\delta x_{\max} = \delta y_{\max} = \delta z_{\max} = 0.09$. The results of our calculation, carried out for different values of R_t (the Rayleigh number), r^* (viscosity ratio) and initial flow pattern are presented in table 3. The table gives the flow patterns, root-mean-square velocity v_{rms}, and Nusselt number *Nu* for the final steady solution. The table also contains values of *Nu* obtained by Busse & Frick (1985). As can be seen from table 3, our values of *Nu* are consistent with the values of *Nu* obtained by Busse & Frick (1985).

Predictions of convective flow pattern according to the nonlinear stability analysis of Busse & Frick (1985) (see figure 6 of their paper) are summarized in the last two rows of table 3. For example, for case a5 in the table, Busse & Frick (1985) showed that square pattern convection is unstable while roll pattern convection is stable.

This result is consistent with our computation of case a5 which started with square pattern convection and ended with roll pattern convection. As can be seen from table 3, all the convective flow patterns obtained in our numerical simulations are consistent with the predictions of Busse & Frick (1985). (A time marching calculation was carried out for case a7. We did not obtain a final steady-state solution for this case since the growth rate of the instability was so small (about 0.065) that too many timesteps were required. We did, however, show that roll pattern convection is unstable as denoted in table 3.)

To see if our numerical code correctly reproduces the value of the critical Rayleigh number R_c, we plot in figure 13 root-mean-square velocity v_{rms} against Rayleigh number R_t for the case of square pattern convection at $r^* = 11$. As can be seen from figure 13, there is a linear relationship between R_t and v_{rms}. By least-squares fitting, we find that v_{rms} becomes zero at $R_t = 1391 \pm 19$; thus we infer that $R_c = 1391$. This value of R_c is close to 1390, the value obtained in the linear stability analysis of Busse & Frick (1985).

Finally, we carried out a numerical simulation of convection of a constant viscosity fluid in a box of aspect ratios $a_x = 3$ and $a_y = 1.5$ at $R_t = 10^5$ and compared our results with those of Travis, Olson & Schubert (1990*a*). Assumed boundary conditions are (6)–(12). Figure 14 shows the planform of the convection we obtained. The planform is hexagonal with a hot upwelling plume at the centre of the hexagon and sheets of cold sinking fluid along the sides of the hexagon. This planform is the same as the one obtained by Travis *et al.* (1990*a*). The Nusselt number we obtained is 9.41, only 2% smaller than the value (9.58) found by Travis *et al.* (1990*a*). Thus we conclude that our result is consistent with the computation of Travis *et al.* (1990*a*).

REFERENCES

Afrid, M. 1990 Three-dimensional natural convection. PhD dissertation, Rutgers University, The State University of New Jersey.

Anderson, D. L. 1981 Plate tectonics on Venus. *Geophys. Res. Lett.* **8**, 309–311.

Baumgardner, J. R. 1985 Three-dimensional treatment of convective flow in the Earth's mantle. *J. Stat. Phys.* **39**, 501–511.

Bercovici, D., Schubert, G. & Glatzmaier, G. A. 1989*a* Three-dimensional spherical models of convection in the Earth's mantle. *Science* **244**, 893–1016.

Bercovici, D., Schubert, G. & Glatzmaier, G. A. 1989*b* Influence of heating mode on three-dimensional mantle convection. *Geophys. Res. Lett.* **16**, 617–620.

Bercovici, D., Schubert, G., Glatzmaier, G. A. & Zebib, A. 1989*c* Three-dimensional thermal convection in a spherical shell. *J. Fluid Mech.* **206**, 75–104.

Bindschadler, D. L., Schubert, G. & Kaula, W. M. 1990 Mantle flow tectonics and the origin of Ishtar terra, Venus. *Geophys. Res. Lett.* **17**, 1345–1348.

Blankenbach, B., Busse, F., Christensen, U., Cserepes, L., Gunkel, D., *et al.* 1989 A benchmark comparison for mantle convection codes. *Geophys. J. Intl* **98**, 23–38.

Bolton, E. W. & Busse, F. H. 1985 Stability of convection rolls in a layer with stress-free boundaries. *J. Fluid Mech.* **150**, 487–498.

Busse, F. H. 1967 The stability of finite amplitude cellular convection and its relation to an extremum principle. *J. Fluid Mech.* **30**, 625–649.

Busse, F. H. & Frick, H. 1985 Square pattern convection in fluids with strongly temperature-dependent viscosity. *J. Fluid Mech.* **150**, 451–465.

Chandrasekhar, S. 1961 *Hydrodynamic and Hydromagnetic Stability*. Clarendon.

Christensen, U. R. 1984*a* Heat transport by variable viscosity convection and implications for the Earth's thermal evolution. *Phys. Earth Planet. Inter.* **35**, 264–282.

CHRISTENSEN, U. R. 1984*b* Convection with pressure and temperature dependent non-Newtonian rheology. *Geophys. J. R. Astron. Soc.* **77**, 343–384.

CHRISTENSEN, U. & HARDER, H. 1991 Three-dimensional convection with variable viscosity. *Geophysical J. Intl* **104**, 213–226.

CSEREPES, L., RABINOWICZ, M. & ROSEMBERG-BOROT, C. 1988 Three-dimensional convection in a two-layer mantle. *J. Geophys. Res.* **93**, 12009–12025.

GLATZMAIER, G. A. 1988 Numerical simulation of mantle convection: Time-dependent, three-dimensional, compressible, spherical shell. *Geophys. Astrophys. Fluid Dyn.* **43**, 223–264.

HAGER, B. H. & GURNIS, M. 1987 Mantle convection and the state of the Earth's interior. *Rev. Geophys.* **25**, 1277–1285.

HOUSEMAN, G. 1988 The dependence of convection planform on mode of heating. *Nature* **332**, 346–349.

KAULA, W. M. 1980 Material properties for mantle convection consistent with observed surface fields. *J. Geophys. Res.* **85**, 7031–7044.

MACHETEL, P., RABINOWICZ, M. & BERNARDET, P. 1986 Three-dimensional convection in spherical shells. *Geophys. Astrophys. Fluid Dyn.* **37**, 57–84.

PARMENTIER, E. M. & TURCOTTE, D. L. 1978 Two-dimensional mantle flow beneath a rigid accreting lithosphere. *Phys. Earth Planet. Inter.* **17**, 281–289.

PATANKAR, S. V. 1980 Numerical heat transfer and fluid flow. Hemisphere, 197 pp.

RICHTER, F. M. 1978 Experiments on the stability of convection rolls in fluids whose viscosity depends on temperature. *J. Fluid Mech.* **89**, 553–560.

SCHNAUBELT, M. & BUSSE, F. H. 1989 On the stability of two-dimensional convection rolls in an infinite Prandtl number fluid with stress-free boundaries. *Z. angew. Math. Phys.* **40**, 153–162.

SCHUBERT, G., CASSEN, P. & YOUNG, R. E. 1979 Subsolidus convective cooling histories of terrestrial planets. *Icarus* **38**, 192–211.

STENGEL, K. C., OLIVER, D. S. & BOOKER, J. R. 1982 Onset of convection in a variable viscosity fluid. *J. Fluid Mech.* **120**, 411–431.

TRAVIS, B., OLSON, P. & SCHUBERT, G. 1990*a* The transition from two-dimensional to three-dimensional planforms in infinite-Prandtl-number thermal convection. *J. Fluid Mech.* **216**, 71–91.

TRAVIS, B., WEINSTEIN, S. A. & OLSON, P. 1990*b* Three-dimensional convection planforms with internal heat generation. *Geophys. Res. Lett.* **17**, 243–246.

WEERTMAN, J. 1970 The creep strength of the Earth's mantle. *Rev. Geophys. Space Phys.* **8**, 145–168.

WHITE, D. B. 1988 The planforms and onset of convection with a temperature-dependent viscosity. *J. Fluid Mech.* **191**, 247–286.

ZEBIB, A., GOYAL, K. & SCHUBERT, G. 1985 Convective motion in a spherical shell. *J. Fluid Mech.* **152**, 39–48.